Simulating air pollutant dispersion in a Dutch neighborhood using DALES

MSc Thesis

Agatha Zamuner

Delft University of Technology

TU Delft

Simulating air pollutant dispersion in a Dutch neighborhood using DALES

by

Agatha Zamuner

Student Name	Student Number
Agatha Zamuner	5862450

Main Supervisor:	Steven van der Linden
Co-Supervisor:	Roderik Lindenbergh
Project Duration:	January, 2024 - July, 2024
Faculty:	Faculty of Civil Engineering and Geosciences, Delft

TU Delft

Abstract

This study investigates pollutant dispersion from residential wood burning in a neighborhood in Utrecht, Netherlands, employing the Dutch Atmospheric Large-Eddy Simulation (DALES) model under various atmospheric conditions.
Residential wood combustion is a major source of urban air pollution, especially during winter months. This research aims to quantify the distribution and distance traveled by pollutants from their release source. By using DALES, detailed analyses of atmospheric variables and pollutant concentration fields are conducted, providing valuable insights into how atmospheric stability influences pollutant spread.
The results show that atmospheric stability significantly affects pollutant dispersion. Higher pollutant concentrations were generally observed near the surface under stable and very stable conditions as compared to neutral conditions, due to restricted vertical motions that limit the vertical dispersion of pollutants. Additionally, under stable conditions, pollutant concentrations remained elevated farther from the source, affecting residents who do not live close to the emission source. The study also compared the performance of DALES with commonly used Gaussian plume models (GPMs) to evaluate their performance in urban environments and under different atmospheric conditions. Three schemes that provide the dispersion parameters for the GPMs are tested to determine their accuracy in representing the DALES results. The comparison reveals that, while GPMs offer a general overview of pollutant distribution, they often fail to accurately capture concentration decay rates or the spatial extent of the plume.
The study concludes that further research should investigate the impact of atmospheric stability on air pollutant dispersion in urban environments. It also highlights the limitations of Gaussian Plume Models (GPMs), which often simplify processes occurring in the boundary layer. In urban settings, where the urban geometry plays a significant role in pollutant dispersion, DALES proves to be more effective than GPMs, which cannot accurately capture the effects of buildings on the plume.

Contents

Abstract i

1 Introduction 1

2 Theoretical Background 4
2.1 **Stability of the atmosphere** . . . 4
2.2 **Transport and dispersion of pollutants** . . . 6
2.2.1 Influence of atmospheric stability on the dispersion of pollutants . . . 7
2.2.2 Influence of urban area on the dispersion of pollutants . . . 8
2.3 **Gaussian Plume Models** . . . 10

3 Methodology 15
3.1 **DALES** . . . 15
3.1.1 Governing equations . . . 16
3.1.2 Boundary conditions . . . 17
3.1.3 Immersed Boundary Conditions . . . 18
3.1.4 Input files . . . 18
3.2 **Simulation set up** . . . 19
3.2.1 Simulation time . . . 19
3.2.2 Domain size and resolution . . . 19
3.2.3 Atmospheric inputs . . . 19
3.2.4 Emission sources . . . 20
3.3 **Neighborhood** . . . 21

4 Results and Discussion 23
4.1 **Dispersion of pollutants under varying atmospheric conditions** . . . 23
4.1.1 Vertical profiles . . . 23
4.1.2 Average characteristics . . . 25
4.1.3 Horizontal cross-sections . . . 27
4.2 **Comparison between DALES and the Gaussian plume models** . . . 35

5 Conclusions and Recommendations 45
5.1 Conclusions . . . 45
5.2 Recommendations . . . 46

A Vertical profiles of *u* and *v* wind 51

B Rotated plume 53

C GPMs - Source 2 54

1

Introduction

In an effort to address air pollution, the municipality of Utrecht in the Netherlands put a ban on open fires starting January 1, 2025 (**NOS, 2023**[1]). However, it has been questioned whether residential wood burning, rather than open fires, is actually the biggest contributor to overall emissions associated with wood burning.
Residential wood combustion contributes significantly to air pollution in many cities worldwide. Several studies (**Hellén et al. [2008]**, **Oke et al. [2017]**, **Saffari et al. [2013]**) indicate that wood burning is responsible for the emission of various pollutants, including fine particulate matter (PM10 and PM2.5), volatile organic compounds (VOCs), carbon monoxide, and polycyclic organic hydrocarbons (PAHs), posing severe health and environmental risks. Exposure to these pollutants can in fact lead to chronic and acute health issues (**Oke et al. [2017]**).

In this context, a study conducted by **Saffari et al. [2013]** in Thessaloniki during the economic crisis of 2012-2013 highlighted the impact of increased wood consumption on air quality, correlating the increased wood consumption with a 30% rise in concentration of PM2.5 during winter with respect to the previous years. Moreover, this rise in particulate matter was also associated with an increase in mortality and respiratory diseases (**Saffari et al. [2013]**).

The impact of wood burning on air quality becomes particularly important when considering that its usage has been recommended in the past years as a renewable energy source, as stated by **Cincinelli et al. [2019]**. The use of biomass as a renewable energy source in Europe has been constantly increasing over the past years. Burning wood is promoted as a carbon neutral energy source because the amount of CO_2 released during wood combustion is the same amount of CO_2 absorbed by trees through photosynthesis during their growth. However, to sustain this balance, woodlands need to be constantly replaced to prevent depletion of the wood fuel resource and this is not always the case (**Cincinelli et al. [2019]**).

Understanding the dispersion of pollutants near and around buildings is crucial to address the problem of air pollution in urban areas. However, predicting pollutant dispersion has proven to be difficult due to the complex geometry of cities (**Tominaga and Stathopoulos [2013]**). The emission sources in a city originate from multiple locations, making it challenging to identify the single sources. Furthermore, plumes can be perturbed by buildings which create mechanical turbulence, thus enhancing mixing (**Oke et al. [2017]**). Urban street canyons, where streets are surrounded by buildings on both sides, limit the mixing of pollutants. This often results in elevated pollution levels within the urban canyons. Moreover, the airflow in the canyons involves channeling and recirculation, resulting in perturbed wind and pressure fields (**Oke et al. [2017]**).

Given these complexities, measuring and modelling air quality in urban areas is a difficult task. Nonetheless, without such information it is not possible to manage emissions to ensure a good environment for the citizens. Until recently, analytical models such as the Gaussian Plume Model have been used to

[1] https://nos.nl/artikel/2496509-utrechtse-raad-stemt-voor-houtstookverbod-in-buitenlucht

simulate the dispersion of pollutants in urban settings (**Tominaga and Stathopoulos [2013]**). These models enable the calculation of many different cases and scenarios relatively quickly. Because of their simple formulation, Gaussian plume models can in fact run quickly without the need for extensive computational resources. Additionally, they only require a few input parameters such as emission rate, wind speed, and atmospheric stability class. However, Gaussian plume models also come with significant disadvantages. They can only provide an averaged distribution and concentration over a longer period, thus lacking the ability to capture more details such as single peaks (**Lober et al. [2021]**). GPMs rely on empirical dispersion coefficients to represent the spread of pollutants. These coefficients do not always accurately capture the complexities of actual plumes. For instance, the typically used dispersion coefficients might not represent the variability of atmospheric conditions in the real world (**Raznjević [2023]**). Moreover, Gaussian plume models assume a relatively flat and homogeneous terrain. The presence of buildings, trees, and other obstacles significantly influences pollutant dispersion by creating complex airflow patterns that Gaussian models cannot adequately represent. This limitation makes them less reliable in urban settings where the interaction between plumes and built structures is critical (**Oke et al. [2017]**).

Nowadays, “street-scale” Computational Fluid Dynamics (CFD) simulation is being increasingly used to simulate the dispersion of pollutants in urban settings. In CFD simulations, the transport equation of concentration is solved based on the velocity field obtained from the Navier-Stokes Equations. Through CFD simulations, detailed information about the flow and concentration of pollutants can be obtained. The most significant disadvantage of these models is their high computational cost, which can significantly limit their application (**Tominaga and Stathopoulos [2013]**). The main CFD models used for researching air pollution are the Reynolds-averaged numerical simulations (RANS), large-eddy simulations (LES), and direct numerical simulations (DNS). Turbulent motions are fully parametrized in RANS models, resulting in a lower computational cost compared to the other models. This allows for repeated and more comprehensive studies that can include the three basic atmospheric conditions (neutral, unstable, and stable stratification) (**Raznjević [2023]**). LES models provide a partial resolution of turbulence, whereas DNS models can fully resolve turbulent motions. Both LES and DNS simulations prove to be effective in capturing the fluctuating behavior of plumes (**Tominaga and Stathopoulos [2013]**). For this reason, LES and DNS are both more suitable for simulations involving complex geometries and boundary conditions, such as those found in urban environments or around buildings.

Despite CFD being used extensively to investigate the dispersion of pollutants, the research objectives, configurations, boundary conditions, and modelling approaches are often very different (**Tominaga and Stathopoulos [2013]**). This heterogeneity makes it more challenging to evaluate the performance of these models. For instance, some studies focus on idealized urban street canyon with square blocks for housing (**Jandaghian [2018]**, **Raznjević [2023]**), while others consider plumes from elevated industrial chimneys that consequently do not encounter significant obstacles (**Toja-Silva et al. [2018]**). Other studies focus on the dispersion of pollutants from ground sources, such as traffic pollution (**Kurrpa et al. [2018]**, **Murena et al. [2009]**). Additionally, due to the high computational costs, a significant number of studies only investigate the neutral case of the atmosphere, disregarding the stable and unstable case (**Tominaga and Stathopoulos [2013]**).

This research aims to understand the footprint of individual private chimneys in a residential neighborhood in Utrecht and determine how far their pollutants reach. To achieve this, large-eddy simulations (LES) are used, specifically using the Dutch Atmospheric Large-Eddy Simulation (DALES) model (**Heus et al. [2010]**). DALES, recently extended with realistic buildings, represents an exceptional tool for understanding the influence of the urban geometry on the flow of pollutants.
To address the to the main research question, that is understanding the footprint of individual chimneys, different simulations under varying atmospheric conditions are conducted to investigate how atmospheric stability affects pollutant dispersion. Due to rapid surface cooling and longer nighttime hours, winter nights in the Netherlands often exhibit stable conditions. Given that air pollution from residential wood burning is more significant during winter nights in the Netherlands when homes are being heated, the study will focus on a neutral case and two stable cases. Understanding how atmospheric stability impacts the dispersion of pollutants represents the first sub-question.
Furthermore, Gaussian plume models are set up to evaluate how well they perform with respect to the LES model. Concentrations fields obtained from the Gaussian Plume Model (GPM) and the LES model are compared to evaluate the ability of the GPM in capturing plume details. In fact, as mentioned

above, while LES models provide a detailed representation, GPM offers an averaged distribution and concentration of pollutants.

This thesis is structured as follows. Chapter 2 provides a theoretical background to the topics investigated in the thesis. Along with atmosphere stability, the transport and dispersion of pollutants in the boundary layer are discussed. In the second part of this chapter, the Gaussian plume model is introduced and its mathematical formulation is explained. Chapter 3 provides information on DALES, the LES model used in this research. This includes the governing equations, the boundary conditions, and also general details on how buildings have been integrated into the model. Secondly, the simulation setup is introduced, explaining how the three different atmospheric conditions were obtained, and also the choice of grid size and resolution. Chapter 4 presents the results of the analysis. This chapter is split into two distinct parts: in the first part, the influence of atmospheric stability on the dispersion of pollutants is addressed through the use of different plots. In the second part, a comparison between the results from DALES and the GPM is presented to evaluate how the GPM compared to the simulations carried out with DALES. Lastly, Chapter 5 draws conclusions on the research, identifying gaps that could be addressed in the future and providing recommendations for future researchers.

2

Theoretical Background

This chapter begins with an introduction to atmospheric stability, as one of the goals of this research is to understand how atmospheric stability affects pollutants dispersion. The three basic atmospheric conditions will be explained, along with the main physical processes that define these conditions. Following this section, the general mechanisms of pollutant transport and dispersion will be discussed. Given that this study focuses on understanding pollutant transport in an urban environment and under varying atmospheric conditions, Subsections 2.2.1 and 2.2.2 will specifically provide a basic initial understanding of the effects of atmospheric stability and the presence of buildings on pollutant dispersion. Lastly, section 2.3 presents one of the most widely used models for simulating the dispersion of pollutants: the Gaussian plume model (GPM). Its mathematical formulation will be discussed, as well as the parameters required to set up this model. Furthermore, different schemes for calculating lateral and vertical standard deviations of the GPMs are described.

2.1. Stability of the atmosphere

To properly introduce the concept of atmospheric stability, it is essential to first define the boundary layer. It is important to note that in this thesis, the focus is on the atmospheric boundary layer (ABL) over land.

The boundary layer (BL), or atmospheric boundary layer (ABL), is defined by (**Stull [1988]**) as the lowest part of the troposphere that is directly influenced by surface forcing, and that responds to these forcing within an hour or less. Over land, the boundary layer exhibits a clear diurnal cycle primarily driven by solar radiation. This cycle affects nearly all meteorological variables, including temperature, humidity and wind patterns.

The thickness of the boundary layer varies both in time and space, typically ranging from hundreds of meters to few kilometres (**Stull [1988]**). Figure 2.1 shows how the boundary layer typically changes in a day. During daytime, a convective mixed layer (or unstable boundary layer) forms. On the other hand, at night, the boundary layer transitions into a stable boundary layer (SBL) with a residual layer (RL) above. These are further explained below.

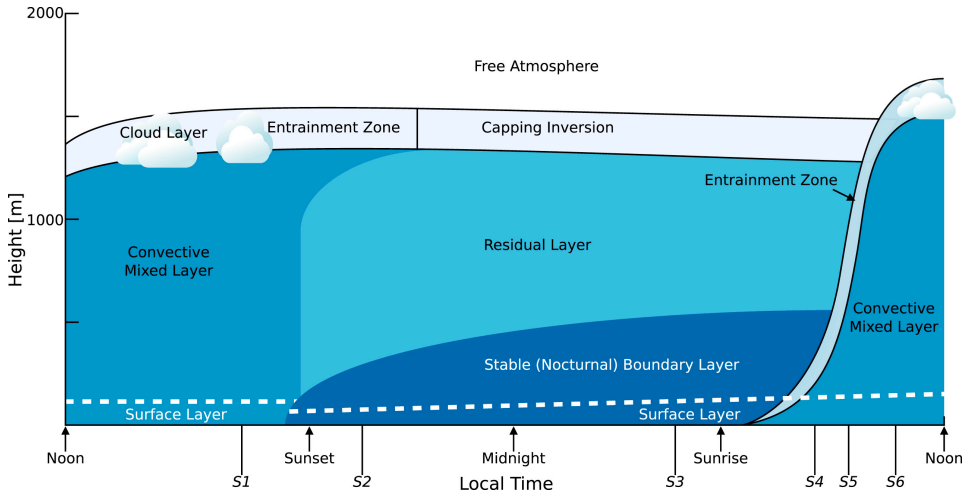

Figure 2.1:
Diurnal evolution of the atmospheric boundary layer over land. The figure was obtained from **Bechtle et al. [2019]** and it was adapted from **Stull [1988]**.

During the daytime, the earth's surface heats up and becomes warmer than the air just above it, leading to a positive heat flux from the surface to the air. This warms the near-surface air, making it lighter than the air aloft. Consequently, the less dense air rises and convection will occur (**van der Linden [2020]**). In this convective boundary layer, vertical turbulent mixing is typically expected, with buoyancy playing a significant role due to rising thermals from the ground surface. This results in the thorough mixing of momentum, potential temperature, water vapor and other scalars, as shown in Figure 2.2. The boundary layer during this time is dynamic and characterized by instability, driven by both buoyant and mechanical turbulence. As the day progresses, this active vertical mixing continues, driven by the continued heating of the surface. By late afternoon, the mixed layer often reaches its maximum depth, extending up to typically 1500 meters (**Stull [1988]**). The mixed BL is usually capped by an inversion layer that marks its upper boundary. Above this inversion, the boundary layer is topped by an entrainment zone, as depicted in Figure 2.1.

During nighttime, the absence of solar irradiation causes the land to cool, emitting more longwave radiation than it receives. Consequently, the net radiation balance (shortwave minus longwave) becomes negative. This results in a negative turbulent flux at the surface, causing the near-surface air to become cool and denser than the air above. This density increase causes air to move downward, suppressing turbulence due to negative buoyancy, and leading to stable density stratification. In this stable boundary layer (SBL), turbulence is weaker and characterized by smaller turbulent eddies. The stability of the boundary layer inhibits vertical mixing, which is only maintained by wind shear (**van der Linden [2020]**). As a result, the growth of the SBL is slow, and its upper boundary often remains poorly defined. In the absence of a temperature inversion, the top of the SBL is typically indistinct, with small eddies and a neutral residual layer present above the SBL (**Stull [1988]**).

Figure 2.2 illustrates idealized vertical profiles of various atmospheric variables including temperature (T), potential temperature (θ), specific humidity (q), and wind magnitude (M), for both unstable and stable boundary layers (BLs). The horizontal wind, denoted as M, is calculated as the square root of the sum of the squares of the eastward (U) and northward (V) wind components, where G represents the geostrophic wind (indicated by the dashed line). During the daytime BL, the horizontal wind is smaller than G due to surface friction. Conversely, during clear nights, away from the surface, the wind can be stronger than G due to inertial effects. This results in the so called 'lowlevel jet' or 'nocturnal jet' (**Holtslag and Steeneveld [2009]**).

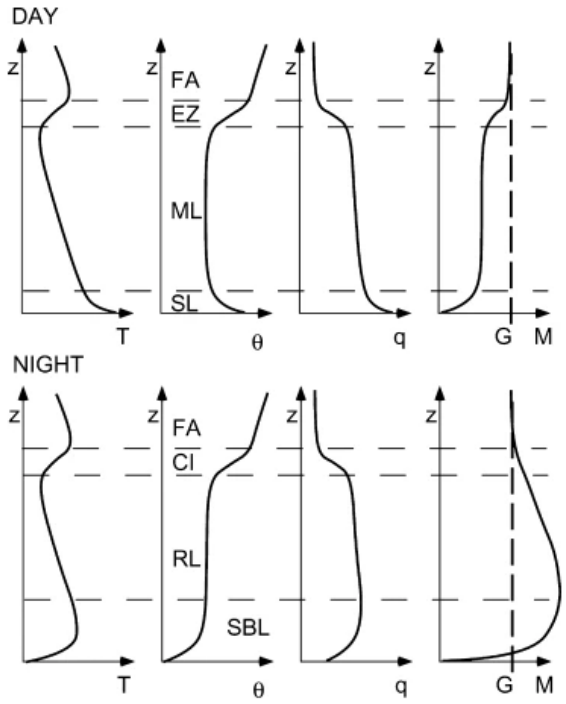

Figure 2.2:
Idealized vertical profiles of mean variables in the atmospheric boundary layer over land in fair weather in the afternoon and around midnight. These variables include temperature (T), potential temperature (θ), specific humidity (q), and wind magnitude (M). The figure was obtained from **Holtslag and Steeneveld [2009]**.

Lastly, the ABL is considered neutral when the potential temperature flux on the surface is nearly negligible (**Liu and Stevens [2022]**). This means there is no buoyancy driving vertical movements in a neutrally stratified BL (**Marshall and Plumb [2007]**). Therefore, turbulence is entirely of mechanical origin, depending on surface friction and the vertical distribution of wind shear. It is noteworthy that, while neutral stability conditions are rarely encountered in the atmosphere, they have frequently been used for studying BL phenomena. This is because neither heating nor cooling need to be considered in a neutral BL, allowing for a simpler representation of some of the processes in the BL.

2.2. Transport and dispersion of pollutants

Figure 2.3 illustrates the primary processes involved in pollutant transport, dispersion, and deposition in the boundary layer.
The mean advection can be regarded as the drifting of air pollutants along with the mean wind. Wind speed has a significant impact on the advection, which can transport pollutants across large distances. Higher wind speeds therefore increase the rate of advection, while they simultaneously enhance the turbulent mixing (**Oke et al. [2017]**).
Turbulence typically involves a number of different sized eddies superimposed on each other. As previously stated, turbulence develops within the BL due to wind shear and buoyancy. The latter only applies to unstable conditions, typically during the day. Near the surface, wind shear dominates as a results of surface drag and the presence of physical obstacles like buildings, trees, and other structures. In strong convective BLs, buoyancy has the strongest contribution due to rising thermals from the ground surface. This process is associated with the formation of eddies whose size is determined by the temperature differences. In other words, the higher the temperature difference, the larger the eddies. These eddies can mix and disperse pollutants vertically. In contrast, in a stable BL thermals of cool and dense air sink, typically inhibiting vertical movements and reducing turbulence. Meanwhile, the developing nocturnal jet increases wind shear, resulting in higher horizontal gradients. This often generates mechanical turbulence. Consequently, turbulence can occur in brief, intense bursts that may

cause mixing throughout the stable boundary layer (SBL) (**Stull [1988]**).
Horizontal transport of air pollutants is typically faster due to higher horizontal wind velocities. On the other hand, vertical transport, which is driven by convection and turbulence, tends to be slower.
Compared to advection, turbulence, and convection, molecular diffusion plays a minor role in pollutant dispersion, affecting their spread only at smaller scales (**Oke et al. [2017]**).
Finally, most pollutants are eventually removed from the atmosphere through gravitational settling, wet deposition, dry deposition, chemical reactions and decay, although these processes are not the focus of this research. For a comprehensive description of these processes, we refer to **Oke et al. [2017]**.

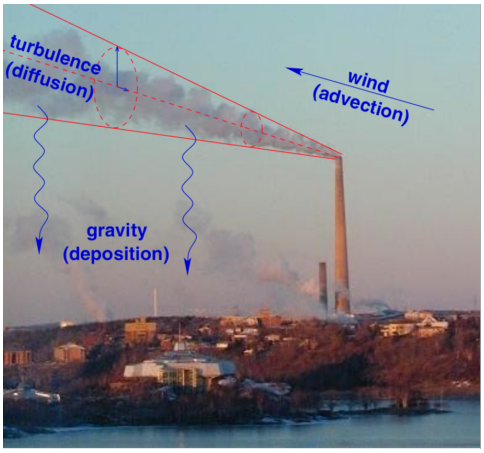

Figure 2.3:
The three main contributions to atmospheric pollutants transport and dispersion. Advection from the mean wind, turbulence through eddies and deposition. The figure was obtained from **Stockie [2011]**.

2.2.1. Influence of atmospheric stability on the dispersion of pollutants

After discussing pollutants transport and dispersion, it is now important to examine the effects of atmospheric stability on these processes. Figure 2.4 displays the different idealized shapes of plumes under varying atmospheric conditions and provides a clear idea on how atmospheric stability plays a role in shaping a pollutants plume.
Starting from the top of Figure 2.4, in unstable conditions, dispersion occurs significantly in the vertical direction, resulting in a looping plume which is characterised by significant up and down movements of the plume. In neutral conditions, a coning plume typically forms. In this case, pollutants can disperse both vertically and horizontally.
Under stable conditions, the plume tends to spread horizontally, with minimal vertical dispersion due to suppressed vertical motions. This is known as fanning and it results in the plume spreading primarily in the horizontal direction rather than vertically.
As mentioned above, an inversion layer can act as a barrier for the pollutants, thus leading to their trapping within the boundary layer. During an inversion, the relative heights of the emission stack and the inversion layer play an important role in the pollution at ground level. Lofting occurs when unstable conditions above the inversion layer allow for the dispersion of a plume, reducing the pollution at ground level. On the other hand, fumigation occurs when a plume is released beneath an inversion layer, meaning a stable stratification is positioned above an unstable or nearly-neutral boundary layer. The pollutants remain trapped in the layer beneath the inversion layer leading to severe air pollution. Moreover, another distinction can be made: if the temperature decreases extremely slowly with height the plume is said to be trapping.

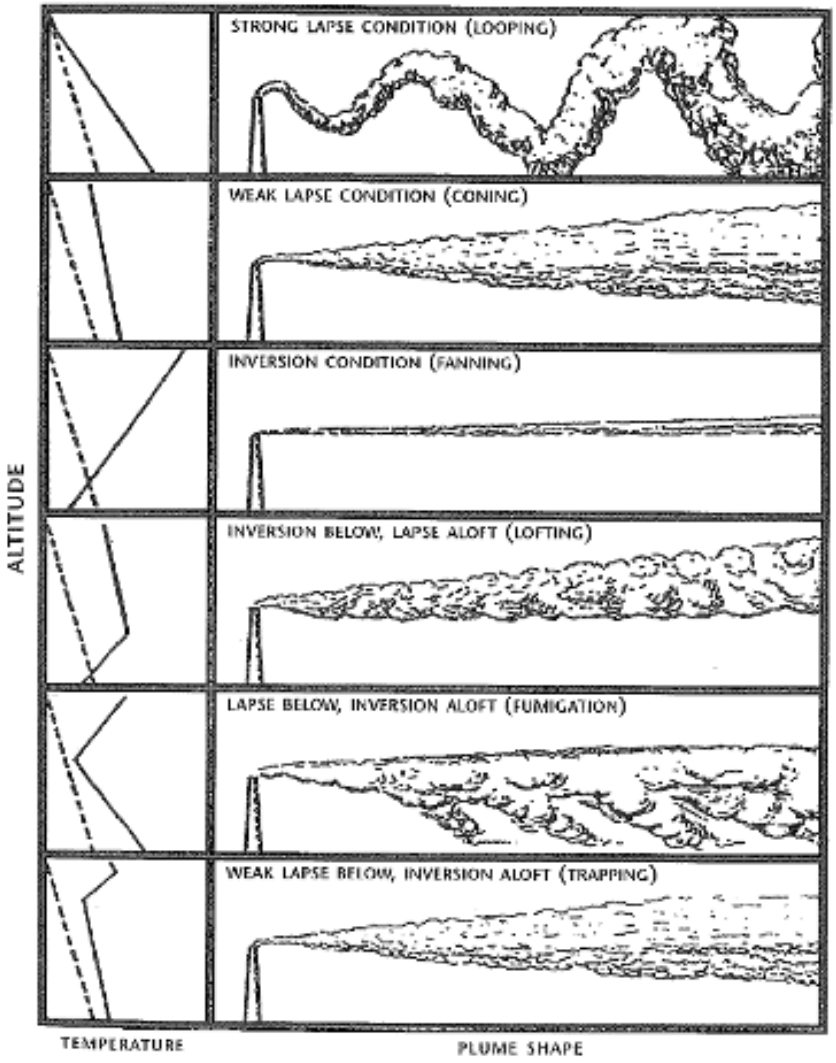

Figure 2.4:
Shape of smoke plumes under varying atmospheric conditions as shown by **Turner and Schulze [2007]**.

2.2.2. Influence of urban area on the dispersion of pollutants

In urban areas, airflow is modified by both the roughness and thermal effects of the city. This includes responses to the layout and design of neighborhoods, the arrangement and orientation of the street network, and the micro-scale effects of buildings, trees, and even moving vehicles, which can all create localized changes in airflow and temperature (**Oke et al. [2017]**).
Oke et al. [2017] describes how airflow is modified in urban areas, starting from the scale of a building (microscale) and progressing up to the scale of an entire urban region. Here, we will review the typical flow patterns in an urban canyon, rather than focusing on the flow around a single building. An overview is given of the concept that may help in understanding results later (shown in Chapter 4).
An urban canyon is a place where the street is flanked by buildings on both sides. When evaluating the type of airflow in an urban canyon, often use is made of the aspect ratio. This height-to-width (H/W) ratio provides a correlation between the height of the buildings and the width of the street (**Zhengtong et al. [2021]**). The highest concentrations of air pollutants are usually found in canyons with high aspect ratios and high traffic volume. This is caused by reduced mixing of air inside the canyon with the atmosphere above, and the high rates of emissions of air pollutants by vehicles.
Concentrations of air pollutants are highly variable, depending on the location within the canyon relative to the direction and magnitude of the approaching flow. Under a simplified case with intermediate aspect

ratios and long streets flanked by buildings of similar height and flat roofs, several flow patterns can be identified, as depicted in Figure 2.5. When the approach flow is perpendicular to the canyon axis, the mean flow creates a recirculation vortex known as a cross-canyon vortex. If the aspect ratio is very large and the flow remains perpendicular to the canyon axis, the main vortex slows and develops into one or more secondary cells toward the floor, known as stacked vortices. When the external wind is at an intermediate angle to the canyon axis, a helical path results, forming a helical vortex. Finally, when the wind direction angle is less than 30°, the flow is channeled along the canyon. If the flow has just entered the end of the canyon, the constriction causes it to accelerate, resulting in a jetting flow.

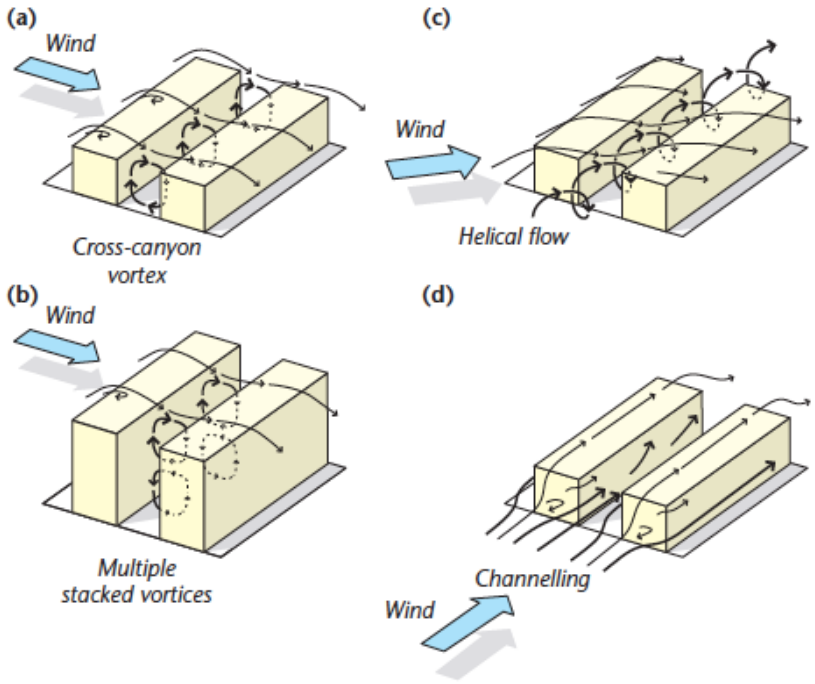

Figure 2.5:
Typical flow patterns in urban canyons. Moving from (a) to (d), the following flow patterns are depicted respectively: cross-canyon vortex, stacked vortices in a deep canyon, helical flow around a canyon and channeling. Figure obtained from **Oke et al. [2017]**.

It is important to understand that these schemes are a simplification. In the real world, other factors come into play: wind directions are not steady, street directions are not orthogonal, street widths vary, canyon aspect ratios are neither symmetric nor continuous, and some streets have trees, balconies, and traffic. This is where the use of fluid dynamics models that handle buildings can provide a more comprehensive understanding of all the processes.

2.3. Gaussian Plume Models

Gaussian plume models (GPM) are a widely used tool for air dispersion calculations. Originally designed for open, flat terrains, GPMs are analytical models which are usually applied to situations with continuous and constant emission rates. They are typically used to model pollutants dispersion over distances ranging from a few hundred of metres to a few kilometers downwind from the emission source (**Oke et al. [2017]**). Gaussian plume models are designed for homogeneous surfaces and therefore cannot accurately capture the behaviour of a plume in an urban setting. While these models can be modified for urban situations, they still often cannot provide accurate information on the behaviour of the plume (**Oke et al. [2017]**). Moreover, although they can estimate the average concentration over longer time period, they cannot predict peak concentrations that occur at shorter turbulent timescale (**Tominaga and Stathopoulos [2013]**). Figure 2.6 shows a schematic representation of a Gaussian plume model, highlighting the key parameters which will be explained further below.

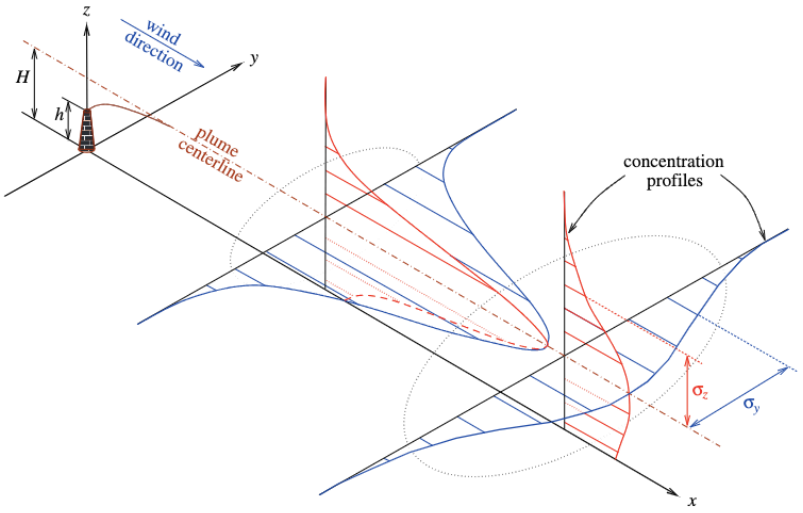

Figure 2.6:
Visual representation of a Gaussian plume model. The plume is emitted from a continuous point source. Profiles of vertical and horizontal concentration are in red and blue respectively. The figure was obtained from **Stockie [2011]**.

The mathematical expression of the Gaussian plume model is:

$$\chi(x,y,z) = \frac{Q}{2\pi u \sigma_y \sigma_z} exp\left(-\frac{y^2}{2\sigma_y^2}\right)\left[exp\left(-\frac{(-z-H)^2}{2\sigma_z^2}\right) + \underbrace{exp\left(-\frac{(-z+H)^2}{2\sigma_z^2}\right)}\right] \tag{2.1}$$

where, $\chi(x,y,z)$ is the concentration at a distance *x* downwind from the source, and cross-wind distance *y* and height *z*. *u* is the mean wind speed (m/s), which is assumed constant across the depth of the plume. *Q* (g/s) is the source strength and *H* (m) is the effective height of the emission stack, which in this study is taken to be the height of the buildings where the chimneys are located. It is important to clarify that the effective height *H* is defined as the sum of the actual stack height *h* and the plume rise δh that arises from buoyant effects (**Stockie [2011]**).

The spread of the plume is regulated by σ_y and σ_z, which are the lateral and vertical standard deviations of the concentration fields respectively, which increase as we move away from the source. In this formulation it is assumed that all of the pollutant is folded back up into the atmosphere and none is deposited. In other words, as the plume hits the ground, it is reflected back into the air above the ground. This assumption is known as “eddy reflection” (**Abdel-Rahman [2008]**). In Eq. 2.1, this

assumption is represented by the underlined term. The equation can also be simplified to look at the concentrations at ground level, where people live. In this case, the height *z* is set to zero:

$$\chi(x,0,0) = \frac{Q}{2\pi u \sigma_y \sigma_z} exp\left(-\frac{y^2}{2\sigma_y^2}\right)\left[2exp\left(-\frac{z^2}{2\sigma_z^2}\right)\right]. \tag{2.2}$$

Since the σ_y and σ_z regulate the shape of the plume, a proper selection of these variables is crucial. Numerous studies have explored various methods for determining the vertical and horizontal standard deviations in both rural and urban settings, as well as under varying atmospheric conditions (**Carrascal et al. [1993]**). The lateral and vertical standard deviations are typically derived from empirical data obtained from field experiments conducted in different atmospheric conditions. However, it is worth noting that many of these experiments were conducted years ago, raising concerns about the accuracy of the parameters used. In her doctoral thesis, **Raznjević [2023]** discussed the lack of accuracy of these empirical parameters. Based on the results of LES simulations, she revisited these parameters and attempted to get new values for the horizontal and vertical standard deviations.

To account for different atmospheric conditions, the Pasquill stability classes are used to define the parameters needed to compute σ_y and σ_z. These stability classes were developed to describe dispersion conditions using regularly-available, surface-based measurements of wind speed, cloud cover and insolation (**Kahl and Chapman [2018]**). The Pasquill system, initially developed by **Pasquill [1961]**, was later modified by **Gifford [1961]**, **Turner [1967]**, and **Briggs [1973]**, among others, thus maintaining its widespread application in air quality models around the world. This scheme classifies the boundary layer into six stability classes, ranging from extremely unstable (A) to extremely stable (F), as highlighted in Table 2.1.

Class	Stability
A	Extremely unstable
B	Moderately Unstable
C	Slightly Unstable
D	Neutral
E	Stable
F	Very stable

Table 2.1:
Stability classes as defined by **Pasquill [1961]**.

The Pasquill classification system provides a guide for selecting different stability classes, as outlined in Table 2.2. As moisture is not considered in the nighttime simulations, the column containing ”clear nights” is used in this study (see Table 2.2). Based on Table 2.2, given that the average horizontal wind speed is lower than 2 m/s for both the stable and very stable boundary layer (BL) cases, class F should be selected. However, the resulting plumes appeared too narrow compared to the results of the DALES simulations. As a consequence, class E was picked instead. Class D was chosen for the neutral BL case for similar reasons. This will be further analysed in Chapter 4.
It is important to note that the Pasquill stability classes have significant shortcomings (**Kahl and Chapman [2018]**). They are simplistic and overlook important processes affecting atmospheric stability. Additionally, specifying unstable classes (A-C) only during the daytime and stable classes (E-F) at night can be unrealistic, especially in rough terrain where turbulence may be mechanically forced. Moreover, the use of qualitative words such as ”strong” and ”slight” insolation could be misleading. This allowed for flexibility in the choice of stability classes in this study.

	Day			Night	
	Incoming solar radiation			Cloudiness	
u (m/s)	Strong	Moderate	Slight	Cloudy ($\geq$4/8)	Clear ($\leq$3/8)
<2	A	A	B	E	F
2-3	A-B	B	C	E	F
3-5	B	B-C	C	D	E
5-6	C	C-D	D	D	D
>6	C	D	D	D	D

Table 2.2:
Guide to the choice of the Pasquill stability classes. Table obtained from **De Visscher [2013]**.

In this study, three different schemes are used to compute the values of the horizontal and vertical standard deviations. **Carrascal et al. [1993]** provides a detailed comparison between different schemes used to obtain σ_y and σ_z. The objective is to assess which scheme fits this study the best.
Among the different schemes, Briggs formulas represent one of the most commonly used methods to compute σ_y and σ_z (**Briggs [1973]**). Briggs formulas are of the form:

$$\sigma_{y,z} = mx(1+nx)^p \tag{2.3}$$

where the coefficients *m*, *n* and *p* are summarised in Table 2.3 for two kinds of terrain roughness: open country and urban.

	Class	σ_y	σ_z
Open country	A	$0.22x(1+0.0001x)^{-0.5}$	$0.20x$
	B	$0.16x(1+0.0001x)^{-0.5}$	$0.12x$
	C	$0.11x(1+0.0001x)^{-0.5}$	$0.08x(1+0.0002x)^{-0.5}$
	D	$0.08x(1+0.0001x)^{-0.5}$	$0.06x(1+0.0015x)^{-0.5}$
	E	$0.06x(1+0.0001x)^{-0.5}$	$0.03x(1+0.0003x)^{-0.5}$
	F	$0.04x(1+0.0001x)^{-0.5}$	$0.016x(1+0.0003x)^{-0.5}$
Urban	A-B	$0.32x(1+0.0004x)^{-0.5}$	$0.24x(1+0.0010x)^{-0.5}$
	C	$0.22x(1+0.0004x)^{-0.5}$	$0.02x$
	D	$0.16x(1+0.0004x)^{-0.5}$	$0.14x(1+0.0003x)^{-0.5}$
	E-F	$0.11x(1+0.0004x)^{-0.5}$	$0.08x(1+0.00015x)^{-0.5}$

Table 2.3:
Briggs formulas for the dispersion coefficients (**Briggs [1973]**).

Most of other sigma schemes are of the power-law form:

$$\sigma_y = ax^b \tag{2.4}$$

$$\sigma_z = cx^d \tag{2.5}$$

where a, b, c and d are given in Table 2.4. It is important to mention that several tables are available in literature for the coefficients of Eq. 2.4 and Eq. 2.5 for both open country and urban conditions. **Carrascal et al. [1993]** concluded that for urban conditions the best performing scheme is described by **McElroy and Pooler [1968]**. Consequently, it was adopted in this study and the coefficients were summarised in Table 2.4.

Class			x <600 m		x >600 m	
	a	b	c	d	c	d
A-B	1.42	0.74	0.09	1.18	0.07	1.22
C	1.26	0.73	0.09	1.11	0.17	1.01
D	1.13	0.71	0.08	1.08	1.07	0.68
E - F	0.99	0.65	0.08	0.96	1.07	0.55

Table 2.4:
Parameters for the Eq. 2.4 and Eq.2.5 according to **McElroy and Pooler [1968]**.

Thirdly, another scheme was used to compute the lateral dispersion: σ_y is calculated based on the angular width of the plume, as described by **Cramer [1979]**. Although this scheme does not take into account different surface roughness, it has already been used to study the dispersion of pollutants in an urban environment (**Herbschleb [2021]**). Therefore, we opted to try the scheme in this study.

$$\sigma_y = 465.116x \tan\theta \tag{2.6}$$

where θ is:

$$\theta = 0.01745(a - b(ln(x)) \tag{2.7}$$

On the other hand, σ_z is calculated using a power law scheme, according to **Singer and Smith [1966]** .

$$\sigma_z = cx^d \tag{2.8}$$

where a, b, c and d are given in Table 2.5 and Table 2.6. While parameters a and b only depend on the stability class, c and d are also dependent on the distance downwind x (km) from the source.

Class	**a**	**b**
A	24.1670	2.5334
B	18.3330	1.8096
C	12.5000	1.0857
D	8.3330	0.7238
E	6.2500	0.5429
F	4.1667	0.3619

Table 2.5:
Parameters in Eq. 2.7 as given in **Cramer [1979]**

Class	x (km)	c	d
A	0.10 - 0.15	158.08	1.0542
	0.16 - 0.20	170.22	1.0932
	0.21 - 0.25	179.52	1.1262
	0.26 - 0.30	217.41	1.2644
	0.31 - 0.40	358.89	1.4094
	0.41 - 0.50	345.75	1.7283
	0.50 - 3.11	453.85	2.1166
	>3.11	σ_z = 5000 m	
B	0.10 - 0.20	90.673	0.93198
	0.21 - 0.40	94.483	0.98332
	>0.40	109.300	1.09710
C	>0.10	61.141	0.91465
D	0.10 - 0.30	34.459	0.86974
	0.31 - 1.00	32.093	0.81066
	1.01 - 3.00	32.093	0.64403
	3.01 - 10.00	33.504	0.60486
	10.01 - 30.00	36.650	0.56589
	>30	44.053	0.51179
E	0.10 - 0.30	23.331	0.81956
	0.31 - 1.00	21.628	0.75660
	1.01 - 2.00	21.628	0.63077
	2.01 - 4.00	22.534	0.57154
	4.01 - 10.00	24.703	0.50527
	10.01 - 20.00	26.970	0.46713
	20.01 - 40.00	35.420	0.37615
F	0.10 - 0.20	15.209	0.81558
	0.21 - 0.70	14.457	0.78407
	0.71 - 1.00	13.953	0.68465
	1.01 - 2.00	13.953	0.63227
	2.01 - 3.00	14.823	0.54503
	3.01 - 7.00	16.178	0.46490
	7.01 - 15.00	17.836	0.41507
	15.01 - 30.00	22.551	0.32681

Table 2.6:
Parameters in Eq. 2.7 as given in **Cramer [1979]**)

3

Methodology

This chapter elaborates on the model used in this study and on how the different simulations were organized. First DALES is introduced, along with some general information about the model, such as its prognostic variables. Afterwards, the governing equations of DALES are discussed, as well as how turbulent motions are treated by the model. In subsection 3.1.2, the boundary conditions are examined, particularly focusing on the changes applied to these conditions for the version of DALES extended with realistic buildings. Next, the immersed boundary condition is addressed in subsection 3.1.3. In subsection 3.1.4, the different input files needed to start a simulation are presented and explained.

Subsequently, an overview of the simulation setup is presented. The choice of resolution and domain size is motivated in subsection 3.2.2, while subsection 3.2.3 elaborates on the changes applied to the physical variables in the input files, necessary to achieve the three different atmospheric conditions. After discussing the changes in the physical variables, details on the two emission sources are provided.

In section 3.3, the location of the neighborhood is presented, along with an explanation of its choice. This section also includes information on the sources location, along with a description of how the 3D models of the neighborhood was generated.

3.1. DALES

The high resolution large-eddy simulation model employed in this study is the Dutch Atmospheric Large-Eddy Simulations (DALES), which is currently maintained by researchers from Delft University of Technology, the Royal Netherlands Meteorological Institute (KNMI), Wageningen University and Research, and the Max Planck Institute for Meteorology (**Heus et al. [2010]**). The version used in this research, DALES 4.4, has been recently extended with realistic buildings, enabling us to understand what their influence on the flow of pollutants is (**Witsenboer [2023]**). DALES has been used to study a variety of topics, including studies of shear-driven flow, convective and stable boundary layers, heterogeneous surfaces, dispersion of pollutants, and flow over sloped terrains (**Heus et al. [2010]**).

DALES solves for a number of time-dependent prognostic variables in its simulations. These variables include the velocity components in the three directions u_i (i= x,y,z), the liquid water potential temperature (θ_l), the total water specific humidity (q_t), the rain water specific humidity (q_r), the rain droplet number concentration (N_r), and up to 100 passive or reactive scalars. An additional prognostic variable can be the subgrid turbulence kinetic energy (SFS-TKE, *e*). To decrease simulation time, depending on the subgrid model, calculations of u_i, *e* and θ_l are mandatory, while others are optional (**Heus et al. [2010]**).

In DALES, the total water specific humidity (q_t) is defined as the sum of the water vapor specific humidity (q_v) and is the cloud liquid specific humidity (q_c):

$$q_t = q_v + q_c \tag{3.1}$$

In this study, moisture is not considered. Therefore, both q_v and q_c are considered equal to 0.

The liquid water potential temperature θ_l is defined in its approximated form as:

$$\theta_l \approx \theta - \frac{L_v}{c_p \Pi} q_c \tag{3.2}$$

with the potential temperature being:

$$\theta = T \left(\frac{p_0}{p} \right)^{\frac{R_d}{c_p}} \tag{3.3}$$

Π is the Exner function and it is defined by:

$$\Pi = \left(\frac{p_0}{p} \right)^{\frac{R_d}{c_p}} \tag{3.4}$$

where L_v is the latent heat of vaporization, c_p is the specific heat of dry air at constant pressure, T is the absolute temperature and p_0 is the reference pressure. As a clarification, the potential temperature θ is defined by **Marshall and Plumb [2007]** as the temperature a parcel of air would have if it were expanded or compressed adiabatically from its existing p and T to the standard pressure p_0. The fact that θ is conserved under adiatbatic displacement makes it ideal to study atmosphere thermodynamics. In simulations without moisture, $\theta_l \approx \theta$ which at the surface is equivalent to the absolute temperature T. Therefore, from now on, the term temperature, instead of potential temperature, will be used throughout the research.

DALES operates on an Arakawa C-grid configuration, where pressure, SFS-TKE, and scalars are positioned at the grid cell center, while the three velocity components are situated at the western, southern, and bottom sides of the grid cell (**Heus et al. [2010]**).

3.1.1. Governing equations

DALES, like other LES models, employs the Navier-Stokes equations to simulate turbulent flow. The Boussinesq approximation is assumed, with the reference state θ_0, ρ_0 and p_0 equal to the surface values of liquid potential temperature, density and pressure, respectively. Under most situations in environmental flows, the ratio of density change to the reference density may be assumed small. The Boussinesq approximation allows to simplify the Navier-Stokes equations, ignoring density variations with the exception of the impact of $\Delta\rho$ on buoyancy (**Katopodes [2019]**). The equations simplified through the Boussinesq approximation are then also filtered to separate the large-scale turbulent motions from the small-scale turbulence. The resolved large-scale motions are directly simulated, while the small-scale motions are modeled using subgrid-scale models to account for their effects on the flow. In DALES, the filter width is set to be the grid size. Hence, all the smaller scale turbulent motions are parameterized below the filter width (**Heus et al. [2010]**).

The governing equations of DALES consist of the continuity equation (Eq. 3.5), the approximated Navier-Stokes equations under the Boussinesq approximation (Eq. 3.6), and the filtered equation for scalars (Eq. 3.7).

$$\frac{\partial \widetilde{u_i}}{\partial x_i} = 0 \tag{3.5}$$

$$\frac{\partial \widetilde{u_i}}{\partial t} = -\frac{\partial \widetilde{u_i}\widetilde{u_j}}{\partial x_j} - \frac{\partial \pi}{\partial x_i} + \frac{g}{\vartheta_0}\widetilde{\vartheta_v}\delta_{i3} + F_i - \frac{\partial \tau_{ij}}{\partial x_j} \tag{3.6}$$

$$\frac{\partial \widetilde{\phi}}{\partial t} = -\frac{\partial \widetilde{u_j}\widetilde{\phi}}{\partial x_j} - \frac{\partial R_{uj,\phi}}{\partial x_i} + S_\phi \tag{3.7}$$

where the tildes indicate the filtered mean variables. The z-direction is taken to be normal to the surface, π is the modified pressure (3.8), δ_{ij} the Kronecker delta, and F_i represents other forcings, including large scale forcing and the Coriolis acceleration (3.9).

$$\pi = \frac{\widetilde{p}}{\rho} + \frac{2}{3}e \tag{3.8}$$

$$F_i^{cor} = -2_{\epsilon ijk}\Omega_{j\widetilde{u}k} \tag{3.9}$$

where Ω is the Earth's angular velocity and ϵ_{ijk} is the Levi-Civita tensor. Whereas source terms for scalars are denoted by S_ϕ, the subfilter-scale (SFS) scalar fluxes are denoted by $R_{uj,\phi} = \widetilde{u_j\phi} - \widetilde{u_j}\widetilde{\phi}$. The deviarotic part of the momentum is given by:

$$\tau_{ij} = \widetilde{u_i u_j} - \widetilde{u_i}\widetilde{u_j} - \frac{2}{3} \tag{3.10}$$

where *e* is the subfilter-scale turbulence kinetic energy (SFS-TKE) which is given by the equation 3.11:

$$e = \frac{1}{2}(\widetilde{u_i u_i} - \widetilde{u_i}\widetilde{u_i}) \tag{3.11}$$

The turbulent motions at the subfilter-scale are modeled through an eddy diffusivity as:

$$R_{uj,\phi} = -K_h \frac{\partial \widetilde{\phi}}{\partial x_j} \tag{3.12}$$

$$\tau_{ij} = -K_m \left(\frac{\partial \widetilde{u_i}}{\partial x_j} + \frac{\partial \widetilde{u_j}}{\partial x_i} \right) \tag{3.13}$$

Here, K_m and K_h represent the eddy viscosity and diffusivity coefficients, respectively. In DALES, these coefficients can be modelled in two ways: either as a function of the SFS-TKE *e* (**Deardorff [1974]**), which is the default approach, or using Smagorinsky closure (**Smagorinsky [1963]**). In this research, the second approach is used to model the eddy viscosity and diffusivity coefficients.

3.1.2. Boundary conditions

The boundary conditions determine how the flow interacts with the boundaries of the computational domain. In DALES, a no-slip boundary is assumed at the bottom of the domain for the filtered velocity component. Due to the no-slip condition, DALES also requires a parametrization of the turbulent drag and the exchange of scalars between the surface and the atmosphere. Turbulent fluxes are modelled via the Monin-Obukhov similarity theory which provides a closure relation, known as law of the wall. The theory provides a robust framework for predicting the profiles of quantities like wind speed, temperature, and humidity within the atmospheric surface layer based on a few measurable parameters like surface roughness and heat flux (**Maronga et al. [2020]**). For a comprehensive description of how turbulent fluxes are modeled at the surface, we refer to **Heus et al. [2010]**.

At the top of the domain, the following conditions are applied:

$$\frac{\partial \widetilde{u}}{\partial z} = \frac{\partial \widetilde{v}}{\partial z} = 0 \tag{3.14}$$

$$\widetilde{w} = 0 \tag{3.15}$$

$$\frac{\partial \widetilde{\phi}}{\partial z} = \text{constant in time} \tag{3.16}$$

In the horizontal direction, periodic boundary conditions (PBC) are typically applied throughout the domain. PBC ensures that the variables at corresponding points on opposite boundaries of the domain are equal (**Heus et al. [2010]**). Under PBC, applying local fluxes within a neighborhood can be become

problematic because it allows fluxes from one end of the neighborhood to flow into the opposite side. To address this issue, a new function called strip function is implemented when running simulations with buildings. This function adds an additional layer along the edges of the domain and sets the concentration of scalars to zero within this layer, thus helping in maintaining the integrity and consistency of the numerical simulation (**Witsenboer [2023]**).

3.1.3. Immersed Boundary Conditions

The immersed boundary layer is integrated into the model to simulate the presence of buildings. During each timestep, it calculates the flow without any obstacles and then adjusts the flow at the wall to accommodate the presence of buildings. DALES' equations are modified to account for the presence of buildings, forcing variables as velocities (u, v, and w), turbulent kinetic energy (TKE), and specific concentrations to zero inside the buildings. Additionally, the liquid water potential temperature and the total specific humidity are forced to the set values inside the buildings.
For instance, the velocity of the wind is directed around the buildings rather than through them. Perpendicular velocities to the wall are all equal to zero through a counterforce that forces the momentum to zero. On the flows parallel to the wall, the wall's presence induces a shear effect. While this alters variables near the wall, those farther from the buildings remain unaffected compared to scenarios without buildings (**Witsenboer [2023]**).

3.1.4. Input files

DALES requires specific input files to establish initial and boundary conditions, define geometry and mesh details, set physical parameters, and determine simulation outputs. While some of these input files are mandatory, others are optional. Mandatory input files for the version of DALES extended with realistic buildings are *namoptions*, *prof.inp*, *lscale.inp*, *lsflux.inp*, *ibm.inp*, and *wsv.inp*.

Namoptions contains all the general model settings required to run the simulations. This includes information such as runtime, domain size, resolution, CPU allocation, and the values of the physical variables, which must agree with the values specified in the other input files.
The input file *prof.inp* includes information on the initial vertical profiles of specific atmospheric variables. Specifically, it contains the initial vertical profiles at t=0 of the liquid water potential temperature (θ_l), the total water specific humidity (q_t), the horizontal wind components (u and v), and the turbulent kinetic energy.
Lscale.inp contains all the information of large scale forcings that are assumed to be constant in time. This input file contains values for parameters such as the geostrophic wind and large scale subsidence. In this study, *lsflux.inp* is used to enable time-dependent large scale flux. Reducing the temperature at the end of the simulation in this input file enables surface cooling processes.

For simulating pollutants dispersion in DALES, the files *ibm.inp* and *wsv.inp* are utilized. The *ibm.inp* file represents all the cells in the domain that are to be buildings, where the number in the cells denotes their respective height in meters. On the other hand, *wsv.inp* specifies the locations of emission sources and their emission rates.

3.2. Simulation set up

Three simulation cases are conducted to assess the influence of different atmospheric conditions on the dispersion of pollutants within the neighborhood of interest. These simulations aim to investigate a neutral case and two stable cases, one of which represents extremely stable conditions. The reason for investigating two stable scenarios follows from the knowledge that during winter in the Netherlands, especially on clear and calm nights, the boundary layer tends to be stable, primarily due to radiative cooling as explained in Section 2.1. On the other hand, previous research has traditionally focused on a neutral atmosphere. Hence, investigating a neutral case becomes particularly interesting when comparing the results from this study to previous research.

3.2.1. Simulation time

In a typical scenario, people return to their homes around 17:00 local time in the evening, and fireplaces are often ignited around that time, remaining lit until bedtime. Based on this general scenario, it can be estimated that fireplaces are emitting pollutants for more than six hours. However, to consider different schedules and habits, a runtime of ten hours, or 36 000 seconds, is deemed as a better choice. Additionally, it is essential to allow sufficient time for both the simulation and the physical processes to reach a quasi-steady state, ensuring the accuracy and consistency of the results. The simulation time will be identical for all the three simulations.

3.2.2. Domain size and resolution

Determining the optimal resolution, grid points distribution, and domain size poses a significant challenge in running these simulations. This challenge primarily rises from the risk of the simulations being computationally too expensive. Hence, it is crucial to achieve a balance, ensuring that the resolution is sufficiently high to enable accurate simulations without them being computationally too expensive. The choice of resolution heavily relies on the investigated physical processes.
To address this challenge, an initial horizontal resolution of ten by ten meters is considered, with 128 by 128 grid points. This results in a horizontal domain size of 1280 meters by 1280 meters.

A Stable Boundary Layer (SBL) is characterized by the absence of larger eddies, suppressed vertical motions, and weaker turbulence, along with the formation of smaller scale eddies. To avoid excessively relying on the subfilter-scale model, a higher resolution in the vertical domain is more adequate, as demonstrated by **Holtslag [2006]**. Therefore, a finer resolution is implemented in the two stable cases to better resolve the expected smaller scale eddies. Although a vertical resolution of Δz= 10 meters is adequate for the neutral case, a resolution of 5 meters in the z-direction is also adopted in the neutral case to ease more precise comparisons with the results. With a resolution Δz = 5 , the number of grid points in the vertical direction increases to 256 grid points. Table 3.1 summarizes the information discussed in the paragraph.

	Neutral BL	**Stable BL**	**Very stable BL**
Horizontal resolution	10 x 10 m	10 x 10 m	10 x 10 m
Horizontal grid poits	128 x 128	128 x 128	128 x 128
Vertical resolution	5 m	5 m	5 m
Vertical grid points	256	256	256

Table 3.1:
Horizontal and vertical resolution in the three cases investigated in the research.

3.2.3. Atmospheric inputs

To generate the different scenarios outlined above, changes will be made to certain input variables.
A stable boundary layer is achieved in DALES by prescribing a time-dependent negative temperature at the surface. This is accomplished by cooling the surface by a certain amount of degrees at the end of the simulation, depending on what atmospheric condition is being modelled. Although the initial temperature is set to the same value in all simulations, the temperature after ten hours will vary based on

the specific case being investigated. An initial temperature of 10°C (or 283.15 K) is applied, reflective of a typical value of temperature at around five during a winter night in the Netherlands, as obtained from observations [1].
Table 3.2 highlights the initial and final temperatures for the three different simulation cases. In a neutral atmosphere, the temperature remains constant during the whole duration of the simulation in the lower part of the domain. However, to simulate realistic atmospheric conditions, a lapse rate of 0.03 K/km is applied at 800 meters to limit the unrestricted growth of the BL in neutral conditions. On the other hand, for the stable cases, cooling at the surface is necessary for stable conditions to occur. Therefore, the temperature will be decreased by 3.5 °C/10 hours for the stable case, while for the extremely stable case, the reduction will be even more pronounced. For the extremely stable case the temperature will be decreased by 7°C/10 hours. This method provides a straightforward approach to simulate the cooling of typical winter nights.
Additionally, since pollutant flow around buildings is being simulated, the temperature of the buildings can be also adjusted. The temperature of the wall and roof of the buildings is kept at 284.15 K throughout the simulation.

	Neutral BL	**Stable BL**	**Very stable BL**
Initial temperature	283.15 K	283.15 K	283.15 K
Final temperature	283.15 K	279.65 K	276.15 K
Cooling rate	-	3.5 K/10 hr	7 K/10 hr

Table 3.2:
Initial and final temperature for the three cases investigated.

Wind speed is another variable that can have an influence on the stability of the atmosphere. In fact, higher wind speeds can often lead to stronger turbulence motions, thus promoting more mixing (**Oke et al. [2017]**). In DALES, the wind is regulated through the geostrophic wind speed and direction. The geostrophic wind is defined as the wind velocity that would occur if the horizontal pressure force balances the Coriolis force, thus ignoring turbulent friction. Selecting a correct value for the geostrophic wind is crucial as relatively high wind speeds can enhance vertical mixing. While it is best to avoid higher wind speeds, lower values are not desirable either. Lower wind speeds result in weaker turbulence and in the formation of smaller scale eddies. This implies that the number of turbulent motions parameterized by the model increases, resulting in a smaller percentage of resolved turbulence with respect to the total turbulence. From reanalysis data[1], a value of approximately 5 m/s for the wind speed at the 950 hPa pressure level was obtained. Considering what mentioned above, 5 m/s seems to be a representative value.
Regarding the wind direction, reanalysis data was consulted again. In DALES, the wind in x-direction is specified from west to east and in the y-direction from south to north. During winter months, the wind mostly blows westerly over the Netherlands. Therefore, in this study, the wind will be directed from west to east.

3.2.4. Emission sources

Two sources will be released in the neighborhood investigated, as the model currently allows only for two sources being outputted in the statistics routine. A value of 5 a.u./second is set as emission rate for both sources.

[1] `https://climatereanalyzer.org`

3.3. Neighborhood

A neighborhood within the municipality of Utrecht was selected for this study. As mentioned in the introduction, open fires will be banned within the municipality of Utrecht, effective from January 1, 2025. This forthcoming regulation guided the decision to select a neighborhood there. Emphasis was placed on finding a neighborhood representative of typical residential areas in the Netherlands. Additionally, an area with a straightforward geometric layout was preferred, meaning an area with a simple and clear arrangement of streets and buildings. The neighborhood picked for this study is situated in the north-eastern part of Utrecht, specifically in the Noordoost district. Within the district, an area characterized by abundant residential housing, was ultimately chosen. Spanning approximately 1280 by 1280 meters, it offers an ideal spatial context for the simulation study. Figure 3.1 shows a view of the neighborhood considered in this research.

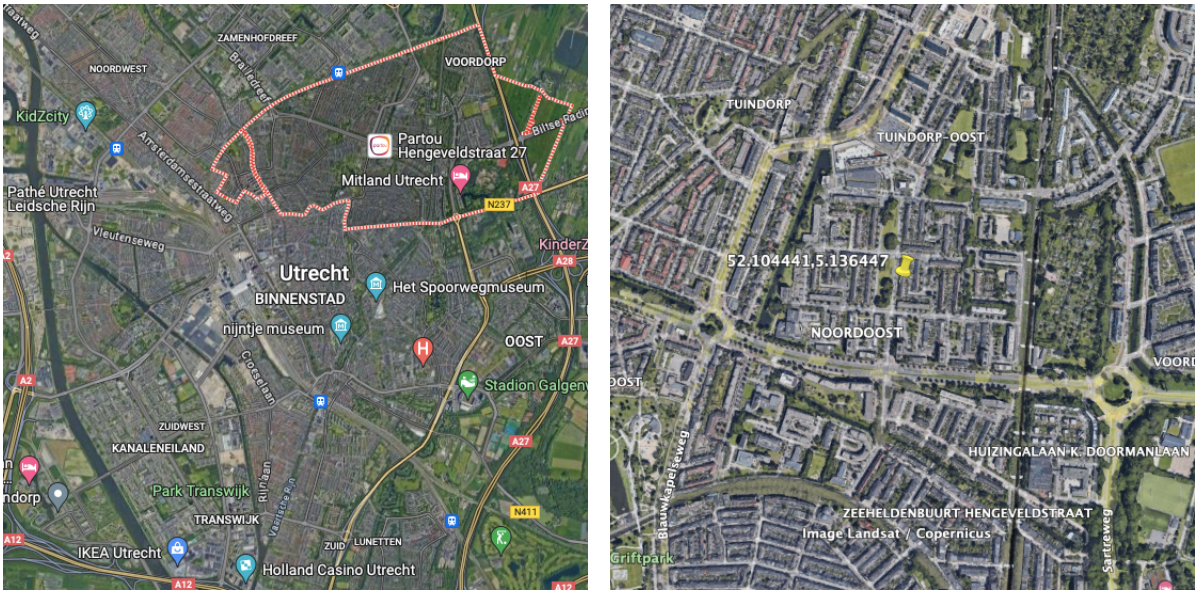

(a) Map of the municipality of Utrecht with the district of Noordoost marked by the red dashed line.

(b) View of the neighborhood used in this research, where the yellow pin marks the centre of the domain.

Figure 3.1:
View of the neighborhood investigated in this research.

Within the neighborhood, two point sources will be released to simulate plumes generated from individual house chimneys. The sources will be placed at the locations where actual chimneys are located, ensuring the simulation reflects real-world conditions. Specifically, the two sources, selected using Google Maps, will be placed at the following geographic coordinates: 52.10361°N, 5.13644°E (Source 1) and 52.10405°N, 5.13777°E (Source 2). Figure 3.2 shows a map of the generated 3D neighborhood where Source 1 is represented by the red circle and Source 2 by the orange one.

Buildings in DALES are created by voxelization, which involves converting a three-dimensional mesh of the urban topography into cubic blocks or 'voxels'. This method allows for the features of the urban environment to be simplified into discrete units that can be more easily processed in simulations.
The 3D urban topography itself is generated using the open-source package City4CFD [2], which is specially designed to process urban topography data for computational fluid dynamics (CFD) simulations (**Paden et al. [2022]**). To accurately model the urban area, City4CFD uses inputs including topographic LiDAR scans (like ANH3) and the surface footprints of buildings. The building footprints are used alongside the LiDAR data to define the boundaries and heights of structures within the simulated environment. Both datasets are public and are available from the Dutch Kadaster [3].

[2] `https://github.com/tudelft3d/City4CFD`
[3] `https://www.pdok.nl`

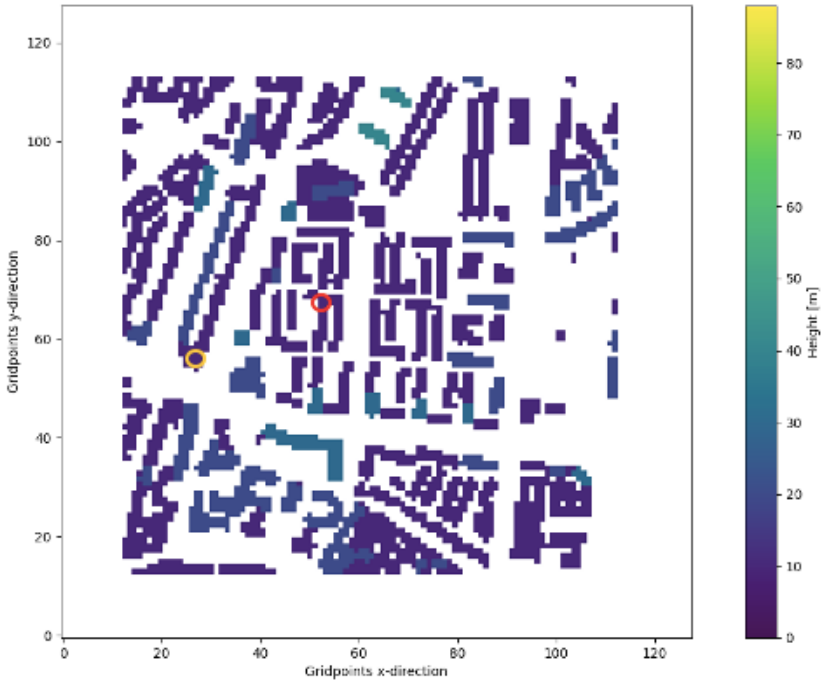

Figure 3.2:
Map of the generated neighborhood at a horizontal resolution of 10 by 10 meters.

4

Results and Discussion

This chapter presents the study's results, along with a discussion. It is divided into two main sections: the first section examines and discusses the effect of different atmospheric conditions on the flow of pollutants in the neighborhood, while the second section focuses on comparing the results of the simulations with the Gaussian plume models.

4.1. Dispersion of pollutants under varying atmospheric conditions

This section explores how atmospheric stability affects pollutant dispersion in the studied neighborhood of Utrecht. Initially, vertical profiles of variables including the *u* and *v* winds and turbulent kinetic energy (TKE) are introduced and analysed. After these vertical profiles, plots of horizontally-averaged characteristics such as the temporal evolution of pollutants concentration for Source 1 and Source 2 are shown.
The second part of the section focuses on comparing wind and concentration fields across the different boundary layers (BLs), uncovering distinct patterns in the data.

Before introducing the different plots, a few clarifications are necessary to avoid confusion and redundancy in the text. The effects of the two sources will always be investigated independently, not cumulatively, and thus will always be plotted separately. Unless otherwise specified, all plots are averaged over the last hour of the simulations. Additionally, "ground level" refers to a height of 2.5 meters. The horizontal cross sections are obtained at four specific levels: 2.5 meters, 7.5 meters, 12.5 meters, and 17.5 meters. Hence, the first level is 2.5 meters, the second is 7.5 meters, the third is 12.5 meters, and the fourth is 17.5 meters. Note also that, the third level (12.5 meters) corresponds to the level (midpoint of cell) into which the pollutant is released.

4.1.1. Vertical profiles

In Figure 4.1 and Figure 4.2, the vertical profiles of the west to east (*u*) wind component and the south to north (*v*) wind component are shown. Under all three atmospheric conditions, both *u* and *v* wind velocities are smaller near the surface due to turbulent friction.
In the neutral boundary layer the *u* wind speed profile increases gradually until 800 meters, which marks the top of the neutral boundary layer. Beyond this point, the *u* wind sharply drops and reaches the constant geostrophic wind speed of 5 m/s.
The stable and very stable boundary layer (BL) cases are characterized by a greater increase in wind speed with height compared to neutral conditions near the surface. The little vertical mixing that characterizes stable conditions results in a much lower boundary layer, and, thus, stronger wind gradients near the surface. The highest *u* wind velocity for the stable and very stable BL is indeed measured below 200 meters.
Both the *u* and *v* vertical profiles of the stable and very stable BL were somewhat expected and match the idealized profiles shown in Section 2.1 (Figure 2.2).

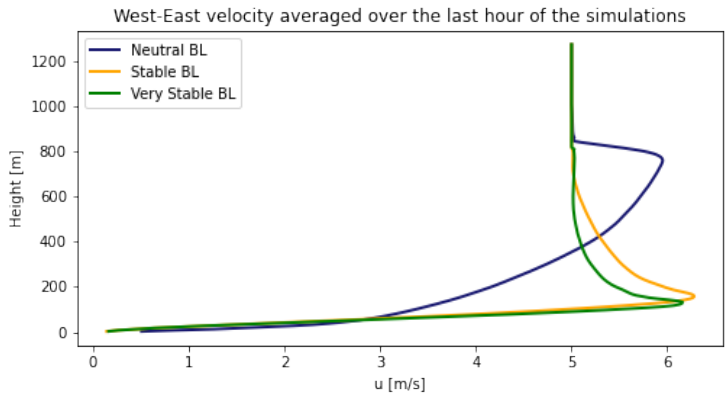

Figure 4.1:
Vertical profile of the west to east (u) wind averaged over the last hour of the simulation for the three basic atmospheric conditions.

The south to north wind (v) velocity was initially set to zero across all the three simulations, but its value changed as the simulations progressed. Under neutral conditions, the velocity steadily increases until reaching its maximum at approximately 250 meters and then gradually decreases until it reaches zero at the top of the neutral boundary layer. Again, higher wind speeds are observed at approximately 100 meters in the stable and very stable cases. Here, the boundary layer is shallower, forcing the wind to change direction (i.e. from W-E to N-S) and to generally reach higher values of the v wind velocities at lower height levels compared to the neutral case.

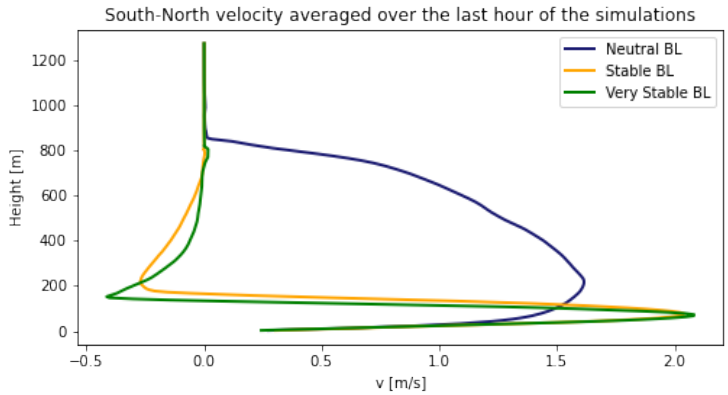

Figure 4.2:
Vertical profile of the south to north (v) wind averaged over the last hour of the simulation for the three basic atmospheric conditions.

Figure 4.3 shows the vertical profile of resolved turbulent kinetic energy (TKE) for all three atmospheric conditions, averaged over the last hour of the simulations. As anticipated, the TKE is higher in the neutral case compared to the two stable cases. The difference can be attributed to the fact that vertical motions are suppressed under stable stratification, inhibiting the formation of turbulence. Moreover, under stable conditions, the thermal contribution to turbulence is minimal or negative due to buoyant forces opposing vertical motion. Consequently, turbulence is primarily mechanically driven but this is typically insufficient to generate high TKE levels (**Oke et al. [2017]**).
When zooming in on the lower levels of the graph, spikes in TKE are observed likely due to the presence of physical obstacles that enhance the production of mechanical turbulence.

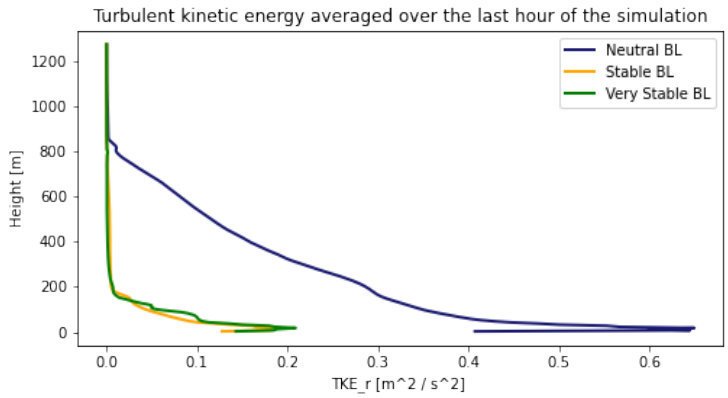

Figure 4.3:
Vertical profile of the resolved turbulent kinetic energy (TKE) averaged over the last hour of the simulation for the three basic atmospheric conditions.

4.1.2. Average characteristics

Figure 4.4 shows the temporal variation of pollutants concentration for Source 1, while Figure 4.5 displays the corresponding variations for Source 2 throughout the duration of the three simulations at the release height (level 3). The domain is horizontally-averaged. In Figure 4.4, the concentration of pollutants in the neutral BL remains within the same range throughout the entire simulation, suggesting that the pollutants are constantly dispersed by vertical mixing in the boundary layer. On the other hand, the stable and very stable BL cases exhibit higher concentrations, with the latter generally showing slightly higher values throughout the simulation duration.

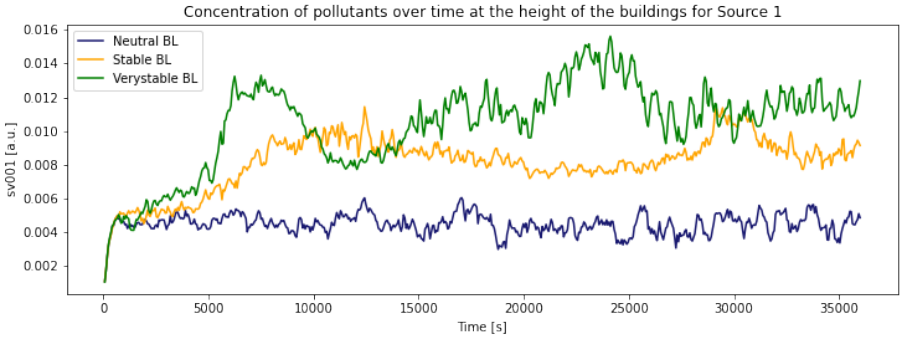

Figure 4.4:
Temporal variation of the concentration of pollutants released from Source 1 over the whole domain.

A similar situation is observed for Source 2, where higher concentrations are still observed under stable and very stable conditions compared to the neutral boundary layer (BL) case. This is due to restricted vertical motions that characterize stable stratification, which limit the vertical dispersion of pollutants and 'trap' them at lower heights.
Comparing Source 1 and Source 2 (Figure 4.4 and Figure 4.5) generally lower concentrations are observed for Source 2. The difference can be attributed to the location within the domain and the distance from the outflow edge, where the concentrations are nudged down. This will also be observed in subsequent plots.

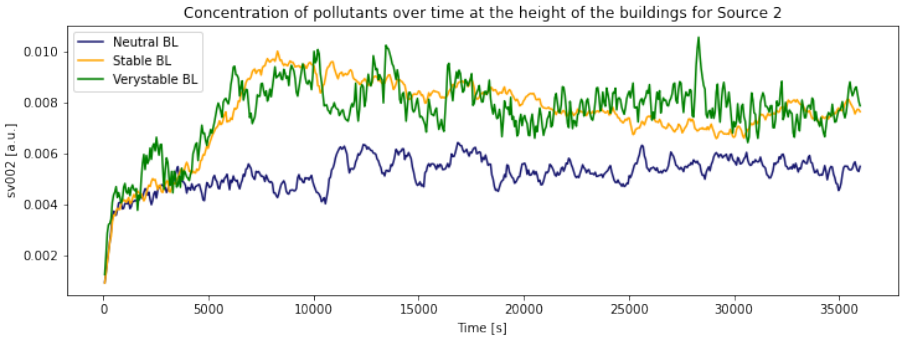

Figure 4.5:
Temporal variation of the concentration of pollutants released from Source 2 over the whole domain.

The vertical profiles of the horizontally-averaged concentrations for Sources 1 and 2 are shown in Figure 4.6. Across all three atmospheric conditions, the concentration drops to zero at approximately 125 meters from the surface and remains zero up to the top of the vertical domain. Therefore, it is more interesting to focus on the lower height levels of the vertical domain for these vertical profiles. Generally higher concentrations are observed at the height of the buildings rather than at the ground level.
When examining Source 1 and Source 2, lower concentrations are observed near the surface under neutral conditions compared to the other boundary layers. However, at higher elevations (around 50 meters for Source 1 and 90 meters for Source 2), the concentrations under neutral conditions become higher than in the two the other cases. This suggests again that the rate of vertical mixing is greater in the neutral case, allowing pollutants to be transported vertically to higher levels.
A marked difference in concentrations near the surface can be observed among the three different atmospheric conditions for Source 1, with the very stable BL case displaying the highest concentrations. When analyzing Source 2, the difference between the three scenarios becomes smaller, as already observed in Figure 4.5.

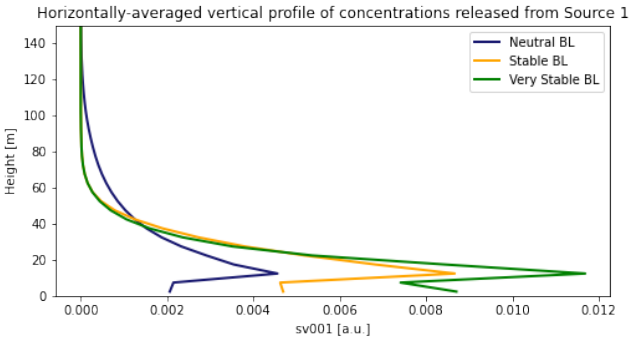

(a)

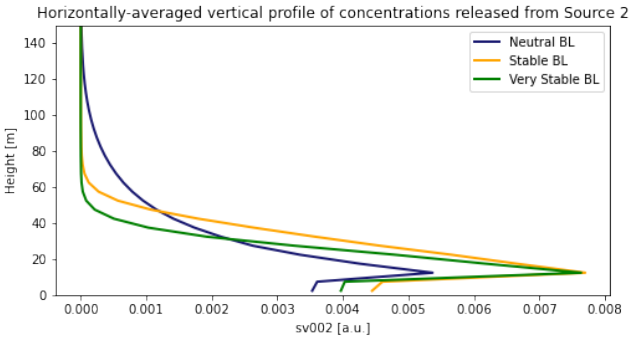

(b)

Figure 4.6:
Vertical profiles of the horizontally-averaged concentrations release from Source 1 (4.6a) and Source 2 (4.6b).

4.1.3. Horizontal cross-sections

In Figure 4.7 a top-view of the west to east (u) and south to north (v) wind fields at ground level is presented for the neutral boundary layer (top), stable boundary layer (middle), and very stable boundary layer (bottom).
At ground level (at 2.5 meters), higher u velocities are generally recorded for the neutral boundary layer, whereas a similar range of v velocities is observed for the three atmospheric conditions up to approximately 20 meters (see Appendix A). Note that higher u wind velocities for the neutral BL are observed up to a a height of approximately 50 meters (see Appendix A). Negative wind speeds are observed for both u and v meaning that the wind changes direction. Generally, the negative velocities are observed in proximity of the buildings.
In all the plots, the influence of the buildings on the wind velocity field is evident. Higher wind speeds are generally observed on average in areas with fewer buildings, while regions with more buildings, such as at the center of the domain, register typically lower velocities. However, it should be noted that certain streets experience higher wind speeds, especially in the case of the neutral and very stable BL. This suggests that channeling, which was mentioned in Chapter 2.1, is taking place. A large volume of air moves through a smaller channel, thereby increasing the wind speed and resulting in jetting flow (**Oke et al. [2017]**).
The height of the buildings also plays locally a role in determining wind patterns within the neighborhood. When looking at the three horizontal cross-section of the v wind, negative velocities can be observed in proximity to a building with a height of approximately 40 meters (at approximately x=750 meters and y=1000 meters). Here, the wind at the ground level is forced to change direction from S-N to N-S. As the wind hits the building, part of the flow is deflected downward and changes direction at the ground. This results in a region of negative velocities.

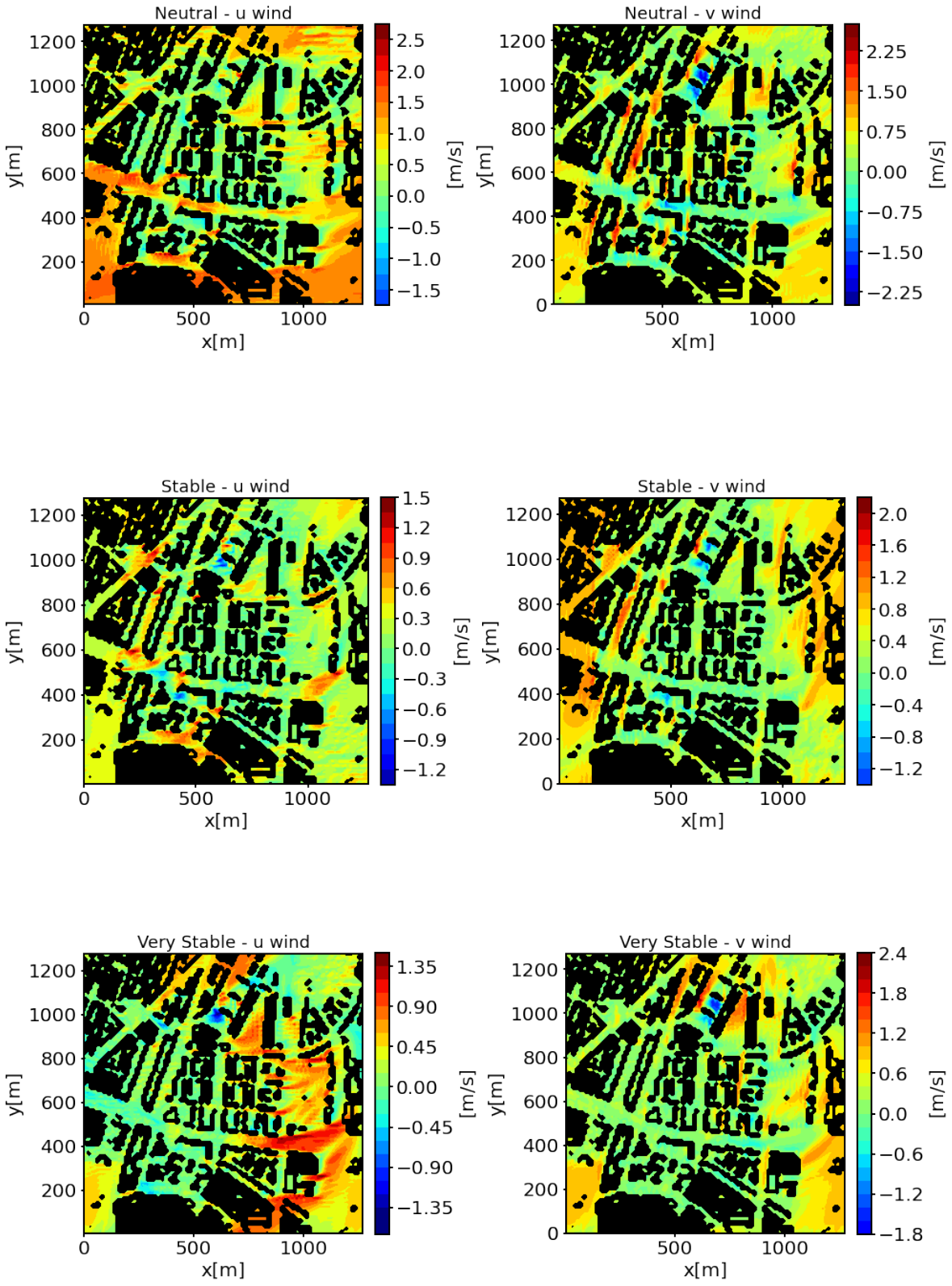

Figure 4.7:
Top view of wind velocity fields for different BL cases. From top to bottom: neutral, stable, and very stable BL. Each subfigure shows west to east (u) wind on the left and south to north (v) wind on the right.

Figure 4.8 shows the concentration fields for the three cases investigated at ground level, with Source 1 on the left and Source 2 on the right. To accommodate the wide range of concentrations, a logarithmic scale was used. This allows a clear visualization of the plume, especially where the concentration values are lower. Contour lines were incorporated to support the visualization and to better quantify the extent of the areas with the highest concentrations. The contour levels range from 10^{-5} to 10^{0}.
It is important to re-mention that the concentrations drop quickly to zero at some distance from the domain boundary, because of the artificial removal of concentration through the implementation of a strip function. This function was introduced in Section 3.1.2.
The impact of buildings is noticeable. The plume is at times visibly forced to flow around the buildings and sometimes becomes trapped in between buildings.
Given that the wind was set to blow from west to east at the beginning of the simulations, the plume direction shifted in all three simulations. This change is more pronounced under stable and very stable conditions than in the neutral case, as confirmed by the wind directions presented in Table 4.1. These wind directions were calculated at the height of the buildings (level 3) at the nearest grid point to the locations of the two sources. Wind direction is indicated relative to the x-axis (i.e., from the east instead of the north). In other words, larger angles suggest that the plume is turning more towards the north. This turning of the plumes to the apparent left (from W-E to S-N) is caused by the turbulent friction, which is not present at the initialization and takes some time to develop. Note that under stable conditions, higher wind gradients can cause the plume to change direction more significantly compared to the neutral BL. In fact, we observed in Figures 4.1 and 4.2 that the boundary layer is shallower under stable conditions, resulting in a greater increase of the *u* and *v* wind velocities with height.

	Neutral BL	**Stable BL**	**Very stable BL**
Source 1	24.65°	51.56°	46.69°
Source 2	26.63°	54.09°	47.86°

Table 4.1:
Wind direction angles computed at the location of the release of Source 1 and Source 2 at the third level (12.5 meters).

Another interesting observation, particularly for Source 2, is the larger spread of the plume under neutral conditions. This indicates higher rates of horizontal dispersion compared to other atmospheric conditions. Moreover, Figure 4.8 shows that the plume spreads horizontally more in the very stable scenario. Under very stable conditions, there is indeed less vertical mixing and it effectively takes longer to mix vertically. Consequently, there is more time for the plume to spread out in the horizontal compared to the stable case. However, it is also possible that pollutants may remain at certain levels where buildings influence the horizontal spreading.

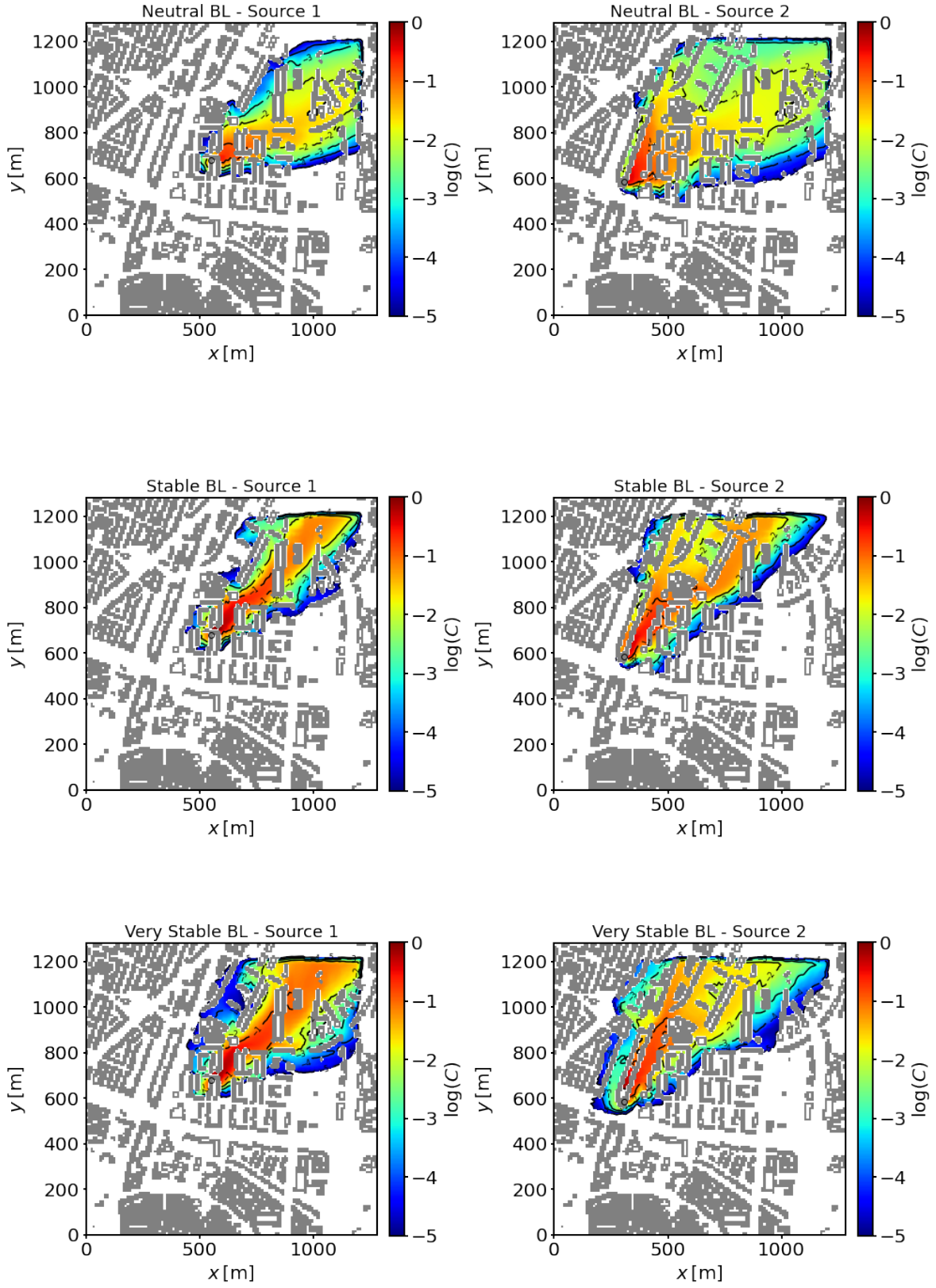

Figure 4.8:
Top view of concentration fields for different BL cases. From top to bottom: neutral, stable, and very stable BL. Each subfigure shows Source 1 on the left and Source 2 on the right.

To quantify the variations in concentration across the three simulations, the area between the 10^{-1} and the 10^{0} contour levels was calculated to verify whether expected lower concentrations were observed in the neutral case. Table 4.2 presents the concentration areas calculated for both sources under the three different atmospheric conditions. Under neutral conditions, both Source 1 and Source 2 exhibit a smaller concentration area compared to the other BL cases, suggesting greater dispersion of pollutants in this scenario both vertically and horizontally.
Stable and very stable conditions show bigger concentration areas, with the very stable BL accounting for the largest areas. This indicates that the decay rate is slower under very stable conditions compared to the other cases.
For Source 1, the difference between the three cases is more pronounced, with the concentration area in the stable case being three times larger than in the neutral case, and the very stable case almost six times larger than the neutral case. The situation is somewhat different for Source 2, possibly due to its location within the domain and its distance from the domain edge where concentrations are forced to zero.

	Neutral BL	**Stable BL**	**Very stable BL**
Source 1	3725 m^2	13665 m^2	18846 m^2
Source 2	8996 m^2	10185 m^2	14120 m^2

Table 4.2:
Areas where the concentrations fall between the 10^{-1} and the 10^{0} contour levels.

Following a visual analysis, we tried to understand how the concentration of pollutants varies when moving away from the different sources. Given that the plumes turned in all simulations, simply moving along the x-axis or y-axis would not yield representative results. Instead, a more effective approach involved calculating the wind direction and moving along that direction.
For Source 1, the wind directions aligned well with the shape and direction of all the plumes. However, this was not the case for Source 2. Therefore, for this quantitative analysis, concentrations were examined along the wind direction line for Source 1. Since this method was not meaningful for Source 2, an alternative approach was taken. A street located to the right of Source 2 was analyzed to observe how concentrations changed along that busy street.
To analyze pollutant dispersion in directions other than the x and y-axes, the original grid was rotated by different angles, depending on whether the analysis followed the wind direction for Source 1 or the busy street close to the release location of Source 2. This rotation process involved shifting the original grid coordinates so that the grid points where the sources were located became the origin in the new grid. A rotation matrix was then used to rotate the grid by the desired angle. Subsequently, concentration values were interpolated from the original grid to a newly defined structured grid in (s, t) space. This new grid spans from -100 to 1000 meters in the 's' direction and from -500 to 500 meters in the 't' direction. 's' is now the distance coordinate from the sources, while 't' is the transverse coordinate. This approach allowed to obtain new concentration values on the new structures grid, facilitating a clearer analysis.
Figure 4.9 shows the variation in pollutant concentrations as one moves away from Source 1 along the wind direction at 12.5 meters. In all three atmospheric conditions, the concentrations rapidly increase after the release, and then start to decrease until it reaches lower values at approximately 200 meters for all boundary layers. The neutral BL case exhibits lower concentrations, with a smaller peak. In contrast, the stable and very stable BL cases exhibit higher concentrations, with the stable BL reaching the highest concentrations among the three scenarios. It is likely that ground-level concentrations (at 2.5 meters) might be higher under very stable conditions, due to limited and slower vertical mixing in this case. This could explain why the concentrations are higher for the stable BL case and this will be further analysed later (see Figure 4.11).

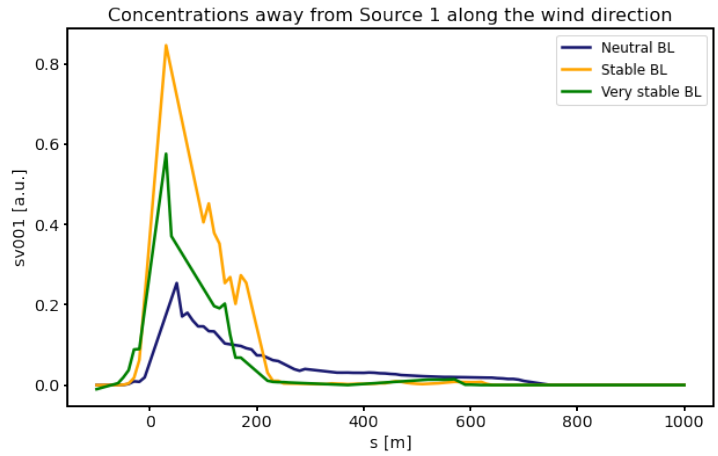

Figure 4.9:
Concentration of pollutants moving along the wind direction from Source 1

When observing the concentrations on the street near Source 2, some differences can be noticed compared to Source 1 (compare Figure 4.10 and 4.9). Initially, higher concentrations are observed in the neutral and stable boundary layers, rather than the very stable BL. A closer look at Figure 4.9 shows that at the beginning of the street, concentrations are lower in the very stable case as the plume seems to be trapped within buildings on the left side of that same street. This could explain why a similar peak is not observed for the very stable conditions compared to the other two cases. However, when moving along the street, concentrations for the very stable case rise at approximately 200 meters, exceeding those in the other two cases. This indicates that farther away from the source the concentration remain higher under very stable conditions. Around 700 meters, all concentrations drop to zero. The reason for that is that a strip function is applied to prevent concentrations from re-entering the domain's lower portion due to periodic boundary conditions. The same was observed in Figure 4.9.

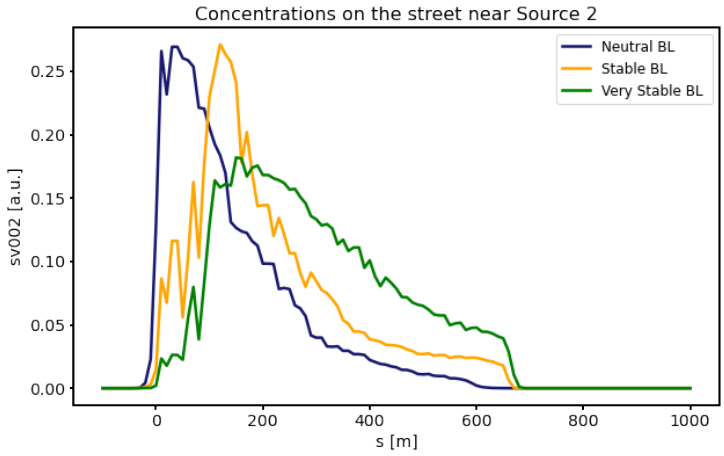

Figure 4.10:
Concentration of pollutants moving along the street in proximity to the release location of Source 2.

Different height levels were examined to understand how the lack of vertical motions can affect the concentrations at different heights. The three different atmospheric conditions were investigated separately, as shown in Figure 4.11. It is important to note that concentrations under neutral and stable conditions were generally higher on this street compared to very stable conditions due to the plume

getting trapped within buildings on the other side of the street in the latter case, hence the different values on the y-axis. In the neutral case, peak concentrations were observed at the release height, indicating significant mixing and a lack of pollutant accumulation near the ground. Conversely, under stable conditions, concentrations near ground level appeared to be higher. In very stable conditions, concentration levels peaked at ground level. This indicates that fumigation may be occurring. This phenomenon was already discussed in Section 2.2.1 where the impacts of different atmospheric conditions on the dispersion of pollutants are introduced. When fumigation occurs, the pollutants remain trapped in lowest levels leading to severe air pollution.

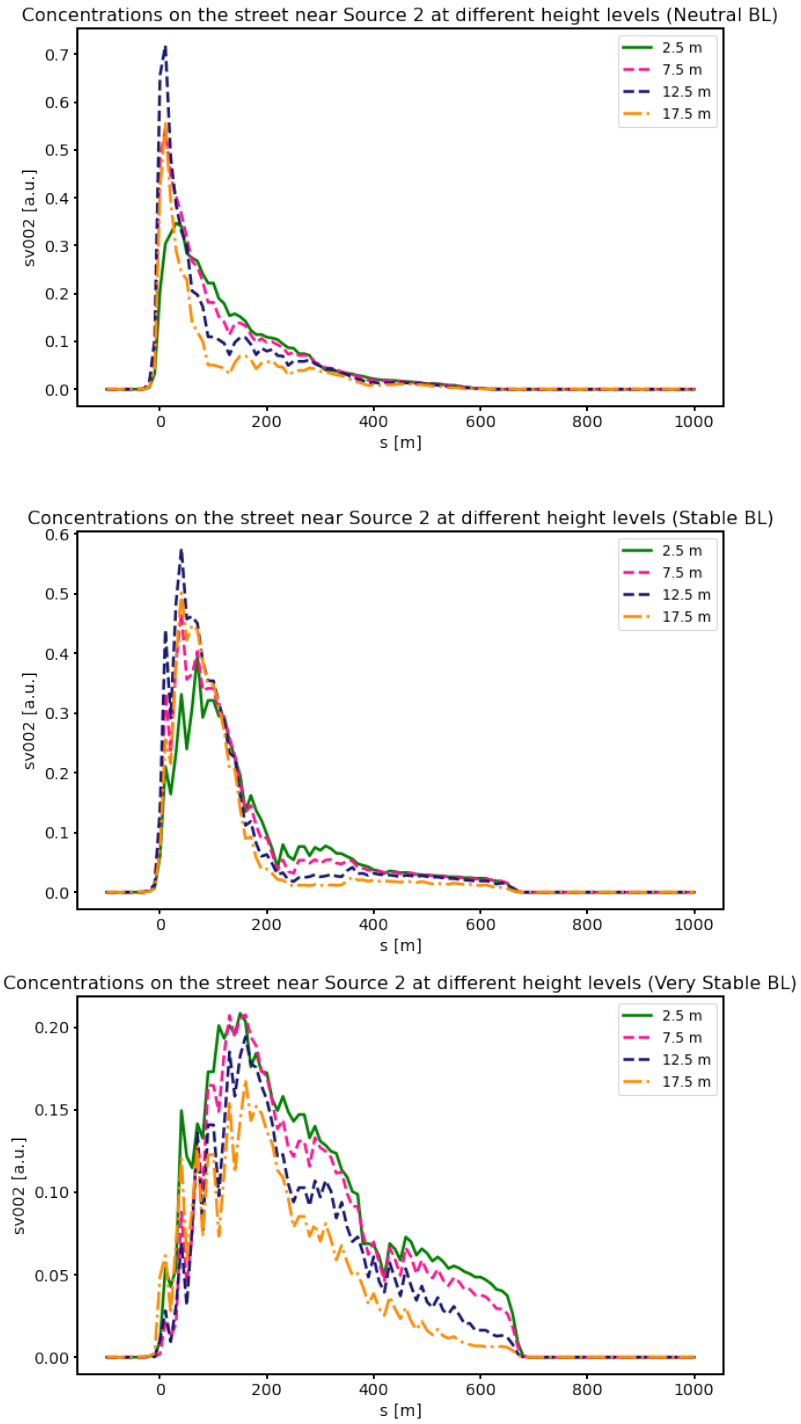

Figure 4.11:
Concentration of pollutants at different height levels moving along the street at the proximity to the release location of Source 2. From top to bottom: neutral, stable, and very stable BL.

4.2. Comparison between DALES and the Gaussian plume models

The Gaussian plume model, as introduced in Section 2.3, requires the choice of various parameters (see Eq. 2.1). Here, their values are introduced.
The effective stack height *H*, which represents the height at which the sources pollution is released, corresponds to 12.5 meters. The *u* wind speed was computed for all three atmospheric conditions at the locations of both sources. Table 4.3 shows the wind speeds used for the different boundary layers and the two sources:

	Neutral BL	**Stable BL**	**Very Stable BL**
Source 1	2.56 m/s	0.88 m/s	1.68 m/s
Source 2	2.59 m/s	0.97 m/s	1.88 m/s

Table 4.3:
Mean wind speeds calculated at Source 1 and Source 2 for the neutral, stable and very stable BLs.

The lateral standard deviations, σ_t and σ_z, were computed using three different schemes introduced in Section 2.3. Schemes by **Cramer [1979], Briggs [1973]**, and **McElroy and Pooler [1968]** were used in this study. Note that from this point on, for simplicity, we will refer to these schemes as Cramer, Briggs, and McElroy (or power-law) schemes.
Determining a value for the emission source *Q* was a bit challenging. In DALES, the emission source is specified in arbitrary units per seconds [a.u./s], making it difficult to relate this unit to real-world measurements. To ensure accurate results, we needed to correlate the Gaussian plume model to DALES. To achieve this, the initial concentration (i.e., at (s,t)=(0,0)) was set to the same value in both the GPM and DALES by equating the prefactor of the GPM to $C_{0,LES}$, which is the concentration averaged over the last hour of the simulation at the grid point where the source was located. Thus, the emission rate *Q* for the Gaussian plume model is now defined via the following relation:

$$\frac{Q}{2\pi\sigma_{t(0,0)}\sigma_{z(0,0)}u} = C_{0,LES} \tag{4.1}$$

Table 4.4 shows the $C_{0,LES}$ for both Source 1 and Source 2 under the three different atmospheric conditions. The values of $C_{0,LES}$ vary a lot among the sources and different conditions. This can be attributed to the fact that in DALES concentrations are averaged within the grid boxes. In this way, the model does not directly account for how much concentration is flowing from one grid box to another. Without accurately capturing the flux of concentrations between grid boxes, the initial concentration may not be completely accurate, thus resulting in very different values of $C_{0,LES}$ between the cases.

	Neutral BL	**Stable BL**	**Very Stable BL**
Source 1	6.97 a.u.	12.12 a.u.	22.98 a.u.
Source 2	3.43 a.u.	3.42 a.u.	31.94 a.u.

Table 4.4:
$C_{0,LES}$ obtained at the locations of the sources release under all three atmospheric conditions.

In Chapter 2.3, the Pasquill classification system, which classifies the boundary layer into six stability classes (A-F), was introduced. Our choice of stability classes slightly differed from those suggested by Pasquill's guidelines. Specifically, class E was selected for the stable and very stable BL cases, while class D was chosen for the neutral case. To verify and further justify our choice, we extracted the lateral standard deviations at 200, 400, and 600 meters from the source for DALES and all the schemes. Table 4.5 presents the lateral standard deviations computed at these distances for the simulations with DALES and GPMs derived from the three different schemes. Note that the three stability classes D, E, and F are listed for the schemes.
In their schemes, **Briggs [1973]** and **McElroy and Pooler [1968]** do not differentiate between class

E and class F. On the other hand, Cramer provides different parameters for the two stability classes, thereby making a clearer distinction between them (see Tables 2.5 and 2.6).
When comparing the values of σ_t for the stable and very stable BLs to class F in the Cramer's scheme, it is evident that class F significantly underestimates the lateral standard deviations. This may result in a plume width that is too narrow, failing to accurately predict the plume's spread. Although class E also underestimates the plume's width, it aligns more closely with the simulations, at least for source 1. Therefore, in this study class E was selected to represent the stable and very stable cases. The same is valid for stability class D in the neutral case, which was preferred over class E.
It can be noticed that Cramer's scheme performs the worst, possibly because there is no distinction between surface roughness, whereas the other schemes differentiate between open country and urban area (see section 2.3). This could suggest that Cramer's scheme struggles to accurately depict the plume's width in urban contexts, even though it has been used in previous studies (**Herbschleb [2021]**). On the other hand, both Briggs and the power-law scheme seem to better capture the plume of the width for the two sources. This will be further investigated below.
Another aspect to note is that all schemes appear to perform worse for Source 2 compared to Source 1. Generally, higher σ_t values are observed for Source 2 compared to the other source. This may once again be related to the location of Source 2 within the domain.

DALES

Neutral BL	Stable BL	Very stable BL
Source 1	Source 1	Source 1
σ_{t200} = 19.68 m	σ_{t200} = 16.03 m	σ_{t200} = 16.85 m
σ_{t400} = 40.09 m	σ_{t400} = 24.34 m	σ_{t400} = 30.39 m
σ_{t600} = 80.36 m	σ_{t600} = 44.69 m	σ_{t600} = 63.23 m
Source 2	Source 2	Source 2
σ_{t200} = 35.34 m	σ_{t200} = 22.11 m	σ_{t200} = 26.30 m
σ_{t400} = 117.59 m	σ_{t400} = 37.57 m	σ_{t400} = 35.31 m
σ_{t600} = 114.82 m	σ_{t600} = 92.29 m	σ_{t600} = 78.85 m

CRAMER

Class D	Class E	Class F
σ_{t200} = 14.91 m	σ_{t200} = 11.14 m	σ_{t200} = 7.40 m
σ_{t400} = 28.83 m	σ_{t400} = 21.56 m	σ_{t400} = 14.33 m
σ_{t600} = 42.11 m	σ_{t600} = 31.40 m	σ_{t600} = 20.94 m

BRIGGS

Class D	Class E-F
σ_{t200} = 29.45 m	σ_{t200} = 20.25 m
σ_{t400} = 58.18 m	σ_{t400} = 40.00 m
σ_{t600} = 85.04 m	σ_{t600} = 58.46 m

MC ELROY

Class D	Class E-F
σ_{t200} = 47.05 m	σ_{t200} = 30.08 m
σ_{t400} = 78.25 m	σ_{t400} = 47.93 m
σ_{t600} = 104.93 m	σ_{t600} = 62.68 m

Table 4.5:
Lateral standard deviations calculated at a distance of 200, 400 and 600 meters from the release location of Source 1 and Source 2. The lateral standard deviations are obtained from DALES (both Source 1 and Source 2), Cramer , Briggs, and McElroy's schemes.

Since the wind directions for Source 2 did not always align well with the shape and direction of the plumes (see subsection 4.1.3), it may be more interesting to focus on Source 1 when comparing the horizontal cross-sections of the plumes from DALES and the GPMs. Figures 4.12, 4.13, and 4.14

present a top-view of the concentration fields for DALES and the Gaussian plume models.
Compared to DALES, all the GPMs exhibit faster decay rates. This is particularly evident in the GPMs obtained from Cramer and Briggs schemes. Starting with the same initial concentration as DALES, the concentrations of the GPMs decrease very rapidly. On the other hand, the power-law scheme maintains higher concentrations over a longer distance, showing a slower decay rate compared to the other schemes. In our case, the McElroy scheme seems most effective in capturing the plumes' decay rate, aligning with **Carrascal et al. [1993]**, which considered it the best performing scheme in urban areas.
The Gaussian plume models assume a constant wind speed and direction and use simplified representations of turbulence, often assuming that dispersion parameters (or the spread of the plume) are functions of downwind distance. In contrast, DALES partially solves for turbulence, thus allowing for a more accurate representation of the transport and dispersion of pollutants. The plume in the simulations are locally more influenced by turbulent friction and also changes of wind speed and direction. Moreover, the dispersion of pollutants in DALES is affected by the presence of 'real' buildings, which can slow down and alter the flow of pollutants. Although Briggs and McElroy schemes are also defined for an urban area, they do not account for the real urban geometry. This could explain the lower concentrations observed in all GPMs.
Furthermore, it should be investigated whether the schemes account for more vertical dispersion. In other words, higher σ_z might be observed in the schemes, indicating that vertical dispersion is higher compared to horizontal dispersion. This will be further discussed in Figure 4.18.

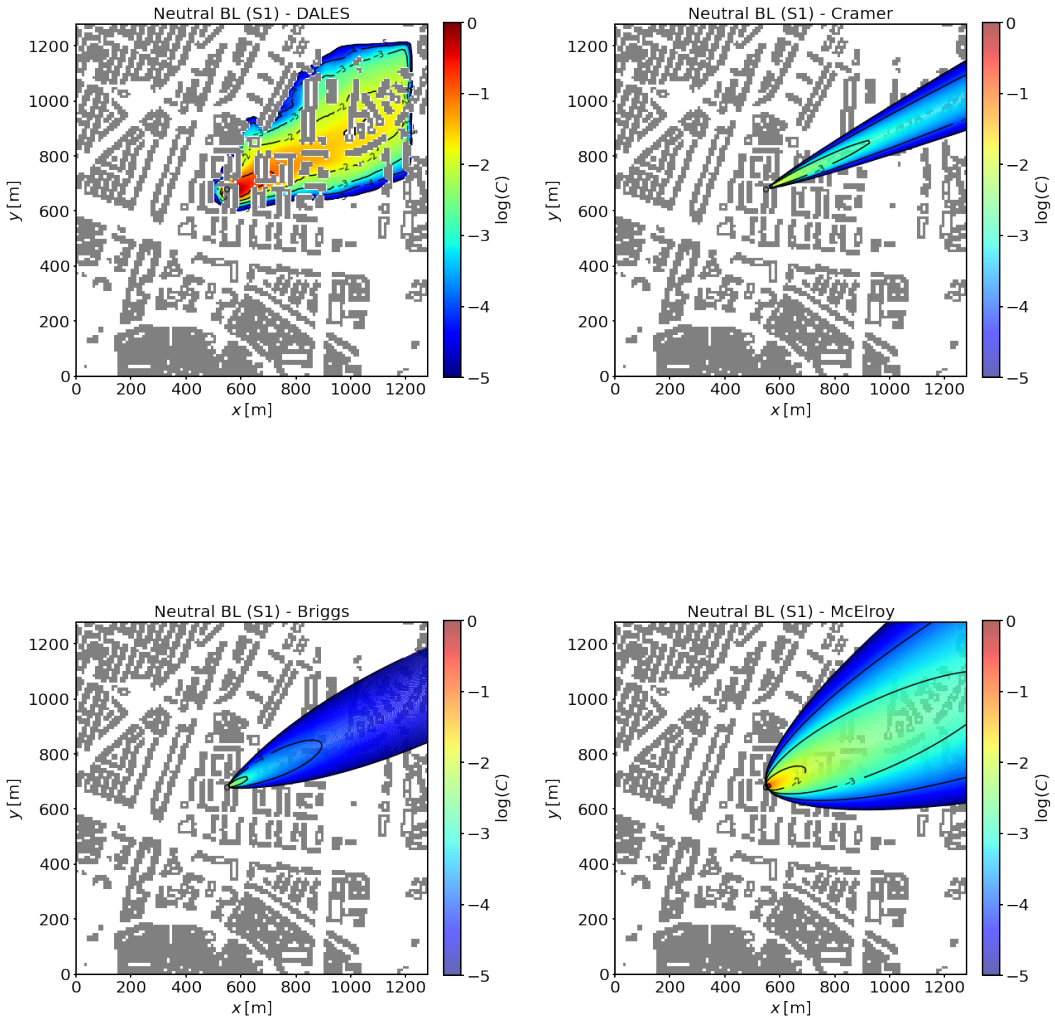

Figure 4.12:
Comparison between DALES and Gaussian plume models for Source 1, under neutral conditions. Top row: DALES (left) and GPM using the scheme by **Cramer [1979]** (right). Bottom row: GPM using the schemes by **Briggs [1973]** (left) and by **McElroy and Pooler [1968]** (right).

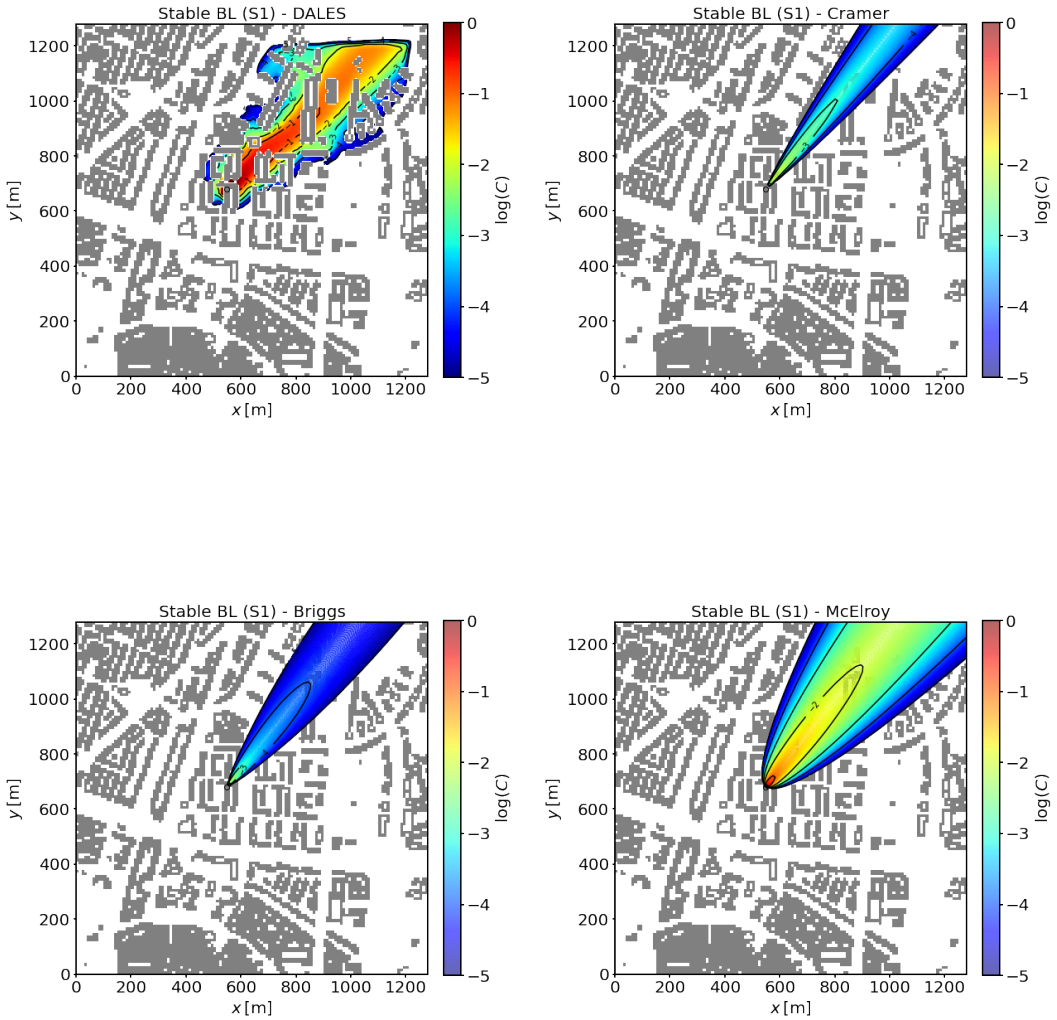

Figure 4.13:
Comparison between DALES and Gaussian plume models for Source 1, under stable conditions. Top row: DALES (left) and GPM using the scheme by **Cramer [1979]** (right). Bottom row: GPM using the schemes by **Briggs [1973]** (left) and by **McElroy and Pooler [1968]** (right).

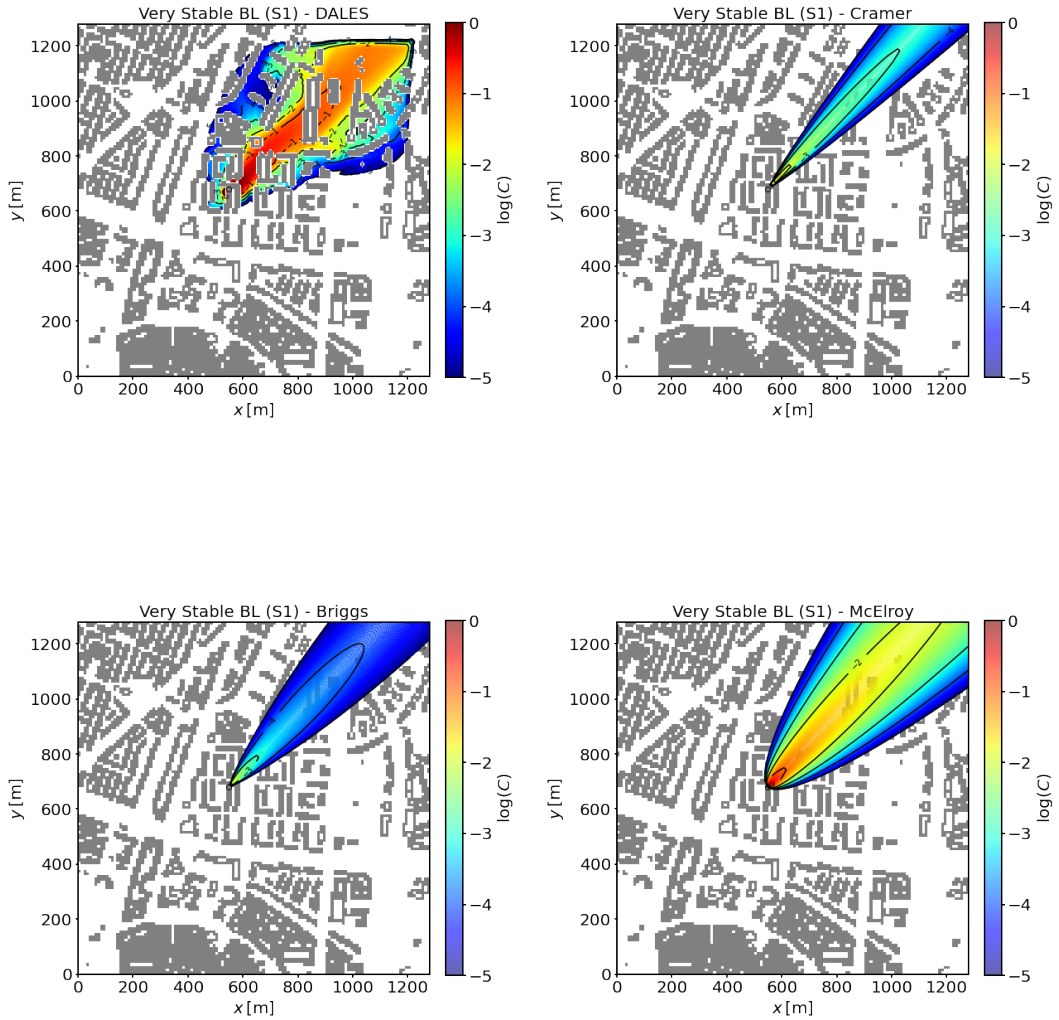

Figure 4.14:
Comparison between DALES and Gaussian plume models for Source 1, under very stable conditions. Top row: DALES (left) and GPM using the scheme by **Cramer [1979]** (right). Bottom row: GPM using the schemes by **Briggs [1973]** (left) and by **McElroy and Pooler [1968]** (right).

Figures 4.15, 4.16, and 4.17 show the horizontal width of the plume as one moves downwind from the source along the *s* direction, covering a range from 0 to 600 meters. The focus on the first 600 meters is due to the influence of the domain's edge on the shape of the plume. When rotated along the s-axis, the plume spreads up to 600 meters and then gets cut off at the edge of the domain (or better at the outflow edge). This is evident in all simulations, and a visual reference can be found in Appendix B. To ensure an accurate analysis, it is therefore better to concentrate on the region up to 600 meters. Within this range, we can observe how the lateral standard deviations (σ_t) vary, depending on whether it is the simulations or the schemes of the GPM.

In figures 4.15, 4.16, and 4.17 the lateral standard deviations obtained from DALES (red line) with those calculated using the three different schemes: Cramer (orange line), Briggs (green line), and McElroy (blue line) are compared. It is immediately evident that Cramer's scheme underestimates the width of the plume for all the boundary layers. This scheme has the lowest horizontal standard deviations, thus

suggesting a much narrower plume compared to the other models.

In the neutral BL, the Briggs scheme initially aligns closely with DALES but diverges slightly as the distance increases. Lastly, the McElroy scheme (blue line) exhibits the highest σ_t values across the distance, constantly overestimating the width of the DALES plume. Overall, the Briggs and McElroy schemes offer a more accurate representation of the plume's width compared to Cramer. It is should be pointed out that even though the σ_t values from Briggs and McElroy in the plots are relatively close to each other compared to Cramer's scheme, there is a significant variation in the decay rates between these schemes (see Figure (4.12)). This could indicate that Briggs' scheme accounts for greater vertical dispersion, potentially leading to higher σ_z values. This could explain the very fast decay rates observed in the GPMs derived from Briggs scheme. Further investigation into this will be provided later in the section.

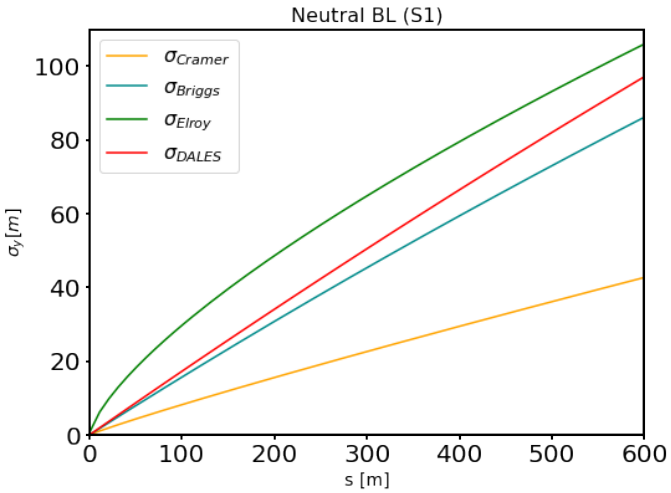

Figure 4.15:
Horizontal plume width as a function of the downwind distance from the source. Plume widths are obtained from the simulations using DALES (red) and from calculations using Cramer (yellow), Briggs (blue) and McElroy (green). Here, the neutral BL is considered.

In a stable BL, the power law scheme shows higher σ_t values compared to both DALES and the schemes across the entire distance. Similar to the neutral BL case, the plume width under stable conditions is overestimated relative to the simulation results. Briggs remains overall the best scheme at capturing the lateral dispersion of the plume. However, it should be noted that the accuracy of the Briggs scheme diminishes at greater distances from the source.

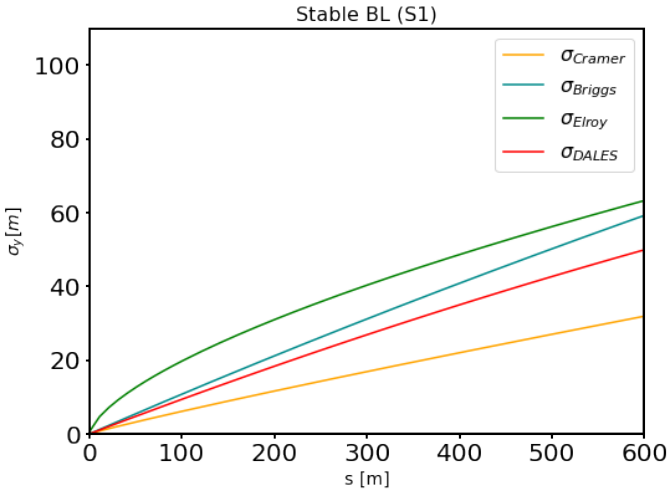

Figure 4.16:
Horizontal plume width as a function of the downwind distance from the source. Plume widths are obtained from the simulations using DALES (red) and from calculations using Cramer (yellow), Briggs (blue) and McElroy (green). Here, the stable BL is considered.

Under very stable conditions, Briggs scheme is more effective at the beginning, while toward the end the power law scheme becomes most accurate in capturing the width of the plume.
Notably, at around 450 meters, DALES demonstrates greater lateral dispersion compared to the GPMs derived from the three schemes. Compared to the stable scenario, the lateral spread σ_t of the plume from DALES is greater under very stable conditions. This agrees with our findings in Section 4.1.3, which indicated that the horizontal spread of the plume was greater in the very stable BL.

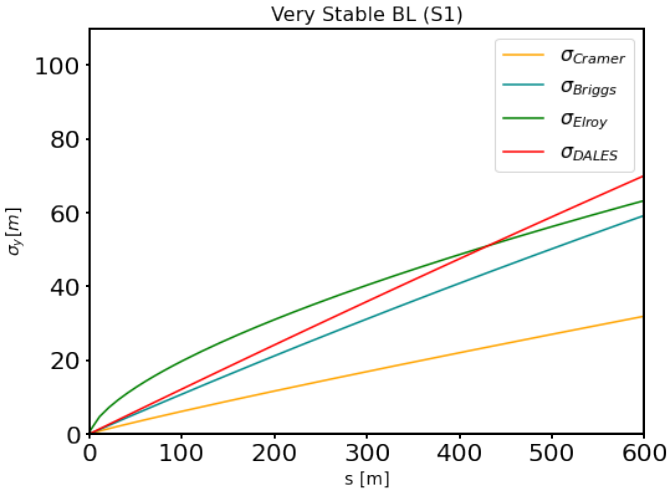

Figure 4.17:
Horizontal plume width as a function of the downwind distance from the source. Plume widths are obtained from the simulations using DALES (red) and from calculations using Cramer (yellow), Briggs (blue) and McElroy (green). Here, the very stable BL is considered.

To further our understanding on the faster decay rates observed in the GPMs, the vertical standard deviations obtained from the three different schemes were examined. Figures 4.18 show the vertical standard deviations (σ_z) as one moves downwind from the source for classes E and F. To avoid rep-

etition, considering that both stable and very stable boundary layer fall under class E, only two plots were created. Plot (a) refers to σ_z under neutral conditions, while plot (b) encompasses stable and very stable conditions.
In both plots, Cramer's scheme consistently displays the smallest vertical standard deviations across the entire range compared to the other schemes. Under neutral conditions (Class D), the power law scheme exhibits the highest vertical standard deviations among all schemes, while Briggs shows slightly lower σ_t. In the stable and very stable BL case, the power law scheme has the highest vertical standard deviations up to a distance of about 350 meters. Beyond approximately 350 meters, Briggs scheme registers the highest σ_t.
This suggests that the fast decay rates observed in the Cramer and Briggs schemes are not a result of greater vertical dispersion within these models. In both Briggs and Cramer schemes, σ_z is as narrow (or even narrower) as σ_t, suggesting that the rapid decay rate in the horizontal cannot be attributed to greater vertical dispersion. Considering the faster decay rate observed in the GPMs derived from the power law scheme, we could have expected lower σ_z values. However, this was not the case. This further suggests that vertical dispersion cannot explain the lower decay rates observed in the GPMs. Most likely, the rapid decline in concentrations observed in the GPMs compared to DALES can be attributed to the fact the GPMs generally assume steady-state conditions with constant wind speeds and directions, while wind velocities and directions are affected by the real buildings and by turbulent friction in DALES.

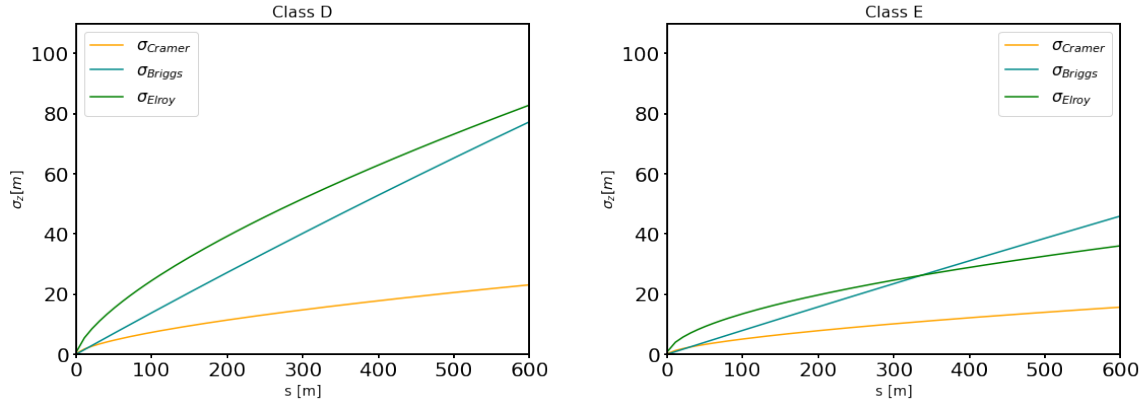

Figure 4.18:
Vertical standard deviations computed for class E and class D.

Figure 4.19 consists of six subplots showing the concentrations profiles along the t-axis under the three different atmospheric conditions. Each subplot compares the concentrations at different distances (100 m, 200 m, 400 m, 600 m) from the source. Across all atmospheric conditions, the peak concentrations decrease with increasing distance from the source. Moreover, greater horizontal dispersion further from the source is observed in all cases, as expected. Under neutral conditions, the most significant dispersion is observed, resulting in wider distributions at greater distances compared to the other cases. Stable and very stable conditions display higher peak concentrations compared to neutral conditions at the same distances. The trend across all plots reinforces our findings that atmospheric stability significantly influences the dispersion of pollutants.
It should be noted that as we move away from the source, the plumes become less centered along the wind direction, likely due to the influence of buildings. This suggests that especially at higher distances from the source, the GPM might fail to predict the spread of the plume.
In all subplots, the highest concentrations are observed at 200 meters rather than 100 meters from the sources under all atmospheric conditions. This can be explained by examining the figures in Appendix B. Around 100 meters from the source, there are numerous buildings along that transect, which could influence the interpolated concentrations observed in this study.

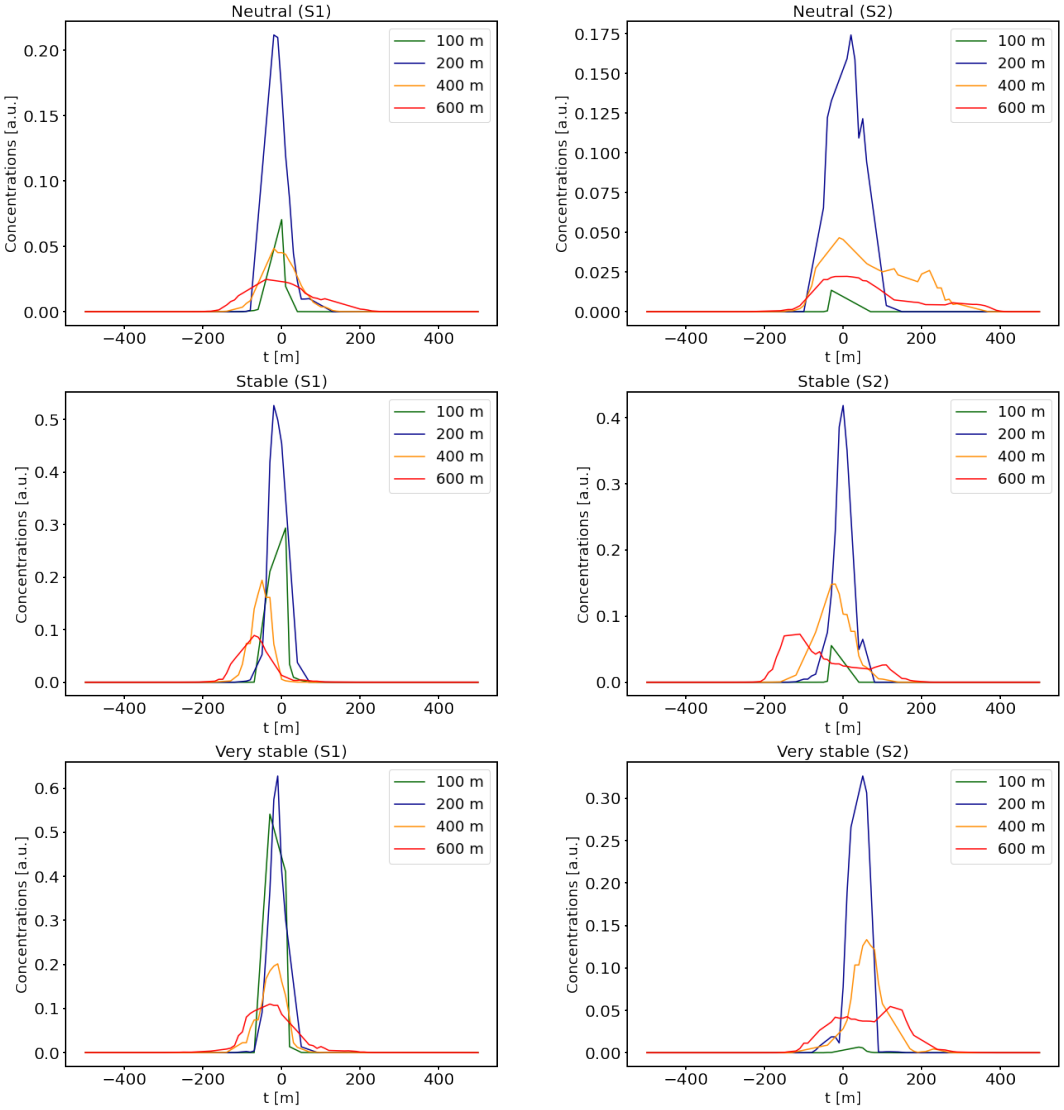

Figure 4.19:
Lateral spread of the plume at a distance of 100 m, 200 m, 400 m, and 600 m from the Source.

5

Conclusions and Recommendations

5.1. Conclusions

The aim of this study was to investigate the dispersion of pollutants in an urban area using DALES. A neighborhood in the municipality of Utrecht, located in the Noordost district and representative of a typical Dutch neighborhood, was selected. The study focused on a typical clear winter night in the Netherlands, with atmospheric variables (e.g. temperature cooling) chosen accordingly. One of the objectives was to determine how atmospheric stability influences pollutant dispersion in the neighborhood, as well as how far pollutants travel and where they end up. Clear winter nights in the Netherlands are typically associated with a stable atmosphere, so two stable cases and one neutral case were examined. The different atmospheric conditions were achieved by cooling the surface by a certain number of degrees according to the desired atmospheric condition.

This study showed that buildings have a clear influence on the wind velocity fields: lower wind velocities are typically observed in areas with more buildings, whereas higher velocities are found in regions with fewer buildings. However, it has been observed that the situation can change locally. Certain streets in the center of the domain exhibited higher wind velocities, most likely due to channeling effects. Channeling occurs when a large volume of air is forced into an urban canyon, where the constriction forces the flow to accelerate and result in higher flow velocities within the canyon. These effects are also reflected in the concentrations observed on those streets, which remain higher compared to other regions.

Throughout the simulations, lower concentrations of pollutants were generally observed near the surface under neutral conditions compared to the two stable cases. Under stable conditions, vertical motions are suppressed, causing pollutants to remain trapped at lower heights and leading to higher concentrations near the surface. Conversely, in a neutral boundary layer, pollutants are dispersed more effectively and can reach higher height levels.
When looking individually at the three different atmospheric conditions, the concentration of pollutants varied at different height levels (2.5 m, 7.5 m, 12.5 m, and 17.5 m), as shown in Figure 4.11. Under stable and very stable conditions, the highest concentrations were recorded at ground level. In contrast, for the neutral boundary layer, the highest concentrations were at the height of the release location (12.5 meters). This is an important factor to consider when managing air pollution, as it suggests that people walking on that street in the neighborhood may be exposed to higher concentrations of these pollutants if the atmosphere is stable.
Furthermore, this study demonstrated that decay rates near the surface decrease slower away from the source for stable and very stable cases compared to neutral conditions. This is supported by the larger concentration areas for the very stable BL case observed in Table 4.2, indicating that pollutants can reach farther distances from the source under stable conditions.

Another objective of this study was to compare the simulation results with Gaussian plume models

(GPMs) to evaluate their accuracy in representing pollutant dispersion. Various schemes were used to create the GPMs to determine which best matched the simulation data. None of the schemes accurately depicted the observed decay rate in the simulations. Briggs and Cramer's GPMs exhibited very fast decay rates, with pollutant concentrations dropping sharply near the release location, while McElroy's GPM had a slower decay rate. In terms of plume width, Briggs and the power law schemes were generally the most effective, whereas Cramer consistently performed poorly, likely because it is not designed for urban environments.
We observed that some schemes estimated the plume width (σ_y) well but produced very low pollutant concentrations, especially Briggs. Plotting vertical standard deviations (see Figure 4.18) revealed that the faster decay rates observed in the GPMs were not due to higher vertical dispersion accounted for by the schemes. Instead, the lower concentrations were likely due to GPMs using a single average wind speed across the entire domain and not accounting for time-varying processes. GPMs fail to capture the fluctuations and variations in wind speed that occur in time. This simplification can lead to inaccuracies because real atmospheric conditions involve changes in wind speed and direction, which affect how pollutants disperse. Additionally, GPMs do not consider the influence of actual buildings, missing the local effects of buildings on pollutant dispersion. By not considering these variations, GPMs might underestimate the actual dispersion and mixing of pollutants, resulting in lower predicted concentrations compared to the DALES.
We also observed that plumes, especially at greater distances from the source, tend to shift from the average wind direction. GPMs cannot capture this shift, making them ineffective for accurately modeling pollutant dispersion when this occurs.
Moreover, we confirmed that the Pasquill stability classification may be limiting, as six stability classes are not sufficient to describe the processes occurring in the boundary layer.

In conclusion, these are all important considerations for municipalities when assessing air pollution and developing new policies or regulations.
DALES has proven to be a valuable tool for studying pollutant dispersion in urban regions. In contrast, the Gaussian plume model (GPM), despite its widespread use, did not always yield accurate results. GPM schemes simplify the processes that occur in the boundary layer. Furthermore, GPMs fail to capture neighborhood-specific dispersion patterns.
GPMs come with several advantages, including cost-effectiveness, ease of implementation, the ability to be used without extensive knowledge, and the fact that they only require a few readily available parameters from observations. As a result of their simplicity, governments, municipalities, and environmental agencies have widely adopted them. However, it can be argued that GPMs may not be sufficient to accurately simulate pollutant dispersion in urban areas under varied atmospheric conditions.

5.2. Recommendations

To further enhance the understanding of pollutant dispersion in urban areas, several recommendations are proposed. First, we observed differences in pollutants concentrations and plume behaviour between Sources 1 and 2, most likely due to their location with respect to the outflow edge. Extending the study to different locations within the domain as well as potentially using larger domains, could provide information about the influence of the outflow edge on the results. Moreover, higher resolution simulations could be employed to capture detailed street-scale effects, allowing for a more accurate observation of the influence of obstacles such as buildings. Additionally, a higher resolution could provide a more accurate depiction of turbulent motions, thereby improving the understanding on pollutant dispersion.
Secondly, we were unable to explore different wind speeds and directions, which could have provided interesting insights into whether similar results would be obtained.
Extracting our own lateral and vertical standard deviations to configure the GPMs, as **Raznjević [2023]** did, could have improved our results. This approach would have been particularly useful, considering that the schemes did not always match the results of the simulations.
For future studies aiming to compare concentrations between DALES and Gaussian Plume Models (GPM), it is important to establish a more accurate correlation between these two methods. This could allow for more precise comparisons and a better understanding of dispersion patterns across the two models.

Currently, DALES does not include gravitational settling, thus assuming that none of the pollutants deposit on the ground. Without accounting for this process, the model might not provide an accurate estimate of concentration and spatial distribution of pollutants in the atmosphere. Incorporating gravitational settling into DALES would provide a more accurate representation of pollutant dispersion and further improve the reliability of simulations.
Future research should include the thermal properties of walls, roofs, and floors, as these can significantly influence pollutant dispersion. Especially if the ambient flow is weak, thermal effect can enhance or diminish flow patters (**Oke et al. [2017]**). This is crucial particularly in urban environments where variations in radiation and heat storage among city elements are prevalent.
Additionally, future studies should consider the impact of atmospheric variables such as moisture, cloudiness, and precipitation to achieve more comprehensive results. These steps would build on current research on the topic.

Bibliography

A. A. Abdel-Rahman. On the atmospheric dispersion and gaussian plume model. In *Proceedings of the 2nd International Conference on Waste Management, Water Pollution, Air Pollution, Indoor Climate, Corfu, Greece*, volume 26, 2008.

P. Bechtle, M. Schelbergen, R. Schmehl, U. Zillmann, and S. Watson. Airborne wind energy resource analysis. *Renewable Energy*, 141:1103–1116, 2019. ISSN 0960-1481. doi: 10.1016/j.renene.2019.03.118.

G. A. Briggs. Diffusion estimation for small emissions. *Atmospheric turbulence and diffusion laboratory*, 965:83–145, 1973.

M. Carrascal, M. Puigcerver, and P. Puig. Sensitivity of gaussian plume model to dispersion specifications. *Theoretical and Applied Climatology*, 48:147–157, 06 1993. doi: 10.1007/BF00864921.

A. Cincinelli, C. Guerranti, T. Martellini, and R. Scodellini. Residential wood combustion and its impact on urban air quality in europe. *Current Opinion in Environmental Science Health*, 8:10–14, 2019. doi: 10.1016/j.coesh.2018.12.007.

H. E. Cramer. *Industrial source complex (ISC) Dispersion Model - User's Guide*. US Dept of Commerce, 1979.

A. De Visscher. *Air dispersion modeling*. John Wiley Sons, September 2013.

J.W. Deardorff. Three-dimensional numerical study of the height and mean structure of a heated planetary boundary layer. *Boundary Layer Meteorology*, 7:81–106, 1974. doi: 10.1007/BF00224974.

F. A. Gifford. Use of routine meteorological observations for estimating atmospheric dispersion. *Nucl. Safety*, 2:47–51, 1961.

H. Hellén, H. Hakola, S. Haaparanta, H. Pietarila, and M. Kauhaniemi. Influence of residential wood combustion on local air quality. *Science of The Total Environment*, 393(2):283–290, 2008. ISSN 0048-9697. doi: 10.1016/j.scitotenv.2008.01.019.

H. Herbschleb. Simulating atmospheric dispersion within the city of eindhoven. Master's thesis, Delft University of Technology, September 2021.

T. Heus, C. C. van Heerwaarden, H. J. J. Jonker, A. Pier Siebesma, S. Axelsen, K. van den Dries, O. Geoffroy, A. F. Moene, D. Pino, S. R. de Roode, and J. Vila-Guerau de Arellano. Formulation of the dutch atmospheric large-eddy simulation (dales) and overview of its applications. *Geoscientific Model Development*, 3(2):415–444, 2010. doi: 10.5194/gmd-3-415-2010.

A. A. M. Holtslag and G. Steeneveld. *Single column modeling of atmospheric boundary layers and the complex interactions with the land surface*. Springer New York, 2009. doi: 10.1007/978-0-387-30440-3_482.

B. Holtslag. Gewex atmospheric boundary-layer study (gabls) on stable boundary layer. *Boundary Layer Meteorology*, 118:243–246, 02 2006. doi: 10.1007/s10546-005-9008-6.

Z. Jandaghian. Flow and pollutant dispersion model in a 2d urban street canyons using computational fluid dynamics. *Computational Engineering and Physical Modeling*, 1(1):83–93, 2018. doi: 10.22115/cepm.2018.122506.1014.

J.D.W. Kahl and H. L. Chapman. Atmospheric stability characterization using the pasquill method: A critical evaluation. *Atmospheric Environment*, 187:196–209, 2018. ISSN 1352-2310. doi: 10.1016/j.atmosenv.2018.05.058.

N.D. Katopodes. Chapter 10 - viscous fluid flow. In *Free-Surface Flow*, pages 324–426. Butterworth-Heinemann, 2019. ISBN 978-0-12-815489-2. doi: 10.1016/B978-0-12-815489-2.00005-8.

M. Kurrpa, A. Hellsten, M. Auvinen, S. Raasch, T. Vesala, and L. Järvi. Influence of residential wood combustion on local air quality. *Atmosphere*, 9(2), 2018. doi: 10.3390/atmos90200659.

L. Liu and R. J. A. M. Stevens. Vertical structure of conventionally neutral atmospheric boundary layers. *Proceedings of the National Academy of Sciences*, 119(22), 2022. doi: 10.1073/pnas.2119369119.

S. Lober, F. Dietrich, and J. Chen. Computational fluid dynamics model to simulate methane dispersion at oktoberfest. *JSG Atmosphere*, 2021. doi: 10.1002/essoar.10506185.1.

B. Maronga, C. Knigge, and S. Raasch. An improved surface boundary condition for large-eddy simulations based on monin-obukhov similarity theory: evaluation and consequences for grid convergence in neutral and stable conditions. *Boundary-Layer Meteorology*, 174:297–325, 2020. doi: 10.1007/s10546-019-00485-w.

J. Marshall and R.A. Plumb. *Atmosphere, ocean and climate dynamics: An Introductory Text*, volume 93. Elsevier, 2007.

J. L. McElroy and F. Pooler. *St. Louis dispersion study*. Number 53. US Department of Health, Education, and Welfare; Public Health Service, 1968.

F. Murena, G. Favale, S. Vardoulaki, and E. Solazzo. Modelling dispersion of traffic pollution in a deep street canyon: Application of cfd and operational models. *Atmospheric Environment*, 43(14): 2303–2311, 2009. ISSN 1352-2310. doi: 10.1016/j.atmosenv.2009.01.038.

T.R. Oke, G. Mills, A. Christen, and J.A. Voogt. *Urban Climate*, volume 8. Cambridge University Press, 2017.

I. Paden, C. García-Sánchez, and H. Ledoux. Towards automatic reconstruction of 3d city models tailored for urban flow simulations. *Frontiers in Built Environment*, 8, 2022. doi: 10.3389/fbuil.2022.899332.

F. Pasquill. The estimation of the dispersion of windborne material. *Meteoro. Mag.*, 90:20–49, 1961.

A. Raznjević. *High-resolution modelling of plume dispersion.* PhD thesis, Wageningen University and Research, 2023.

A. Saffari, N. Daher, C. Samara, D. Voutsa, A. Kouras, E. Manoli, O. Karagkiozidou, C. Vlachokostas, N. Moussiopoulos, M.M. Shafer, J.J. Schauer, and C. Sioutas. Increased biomass burning due to the economic crisis in greece and its adverse impact on wintertime air quality in thessaloniki. *Environmental Science & Technology*, 47(23):13313–13320, 2013. doi: 10.1021/es403847h.

I.A. Singer and M.E. Smith. Atmospheric dispersion at brookhaven national laboratory. *Int. J. Air Water Pollut*, 10(2):125, 1966.

J. Smagorinsky. General circulation experiments with the primitive equations. i. the basic experiment. *Monthly Weather Review*, 91(3):99–164, 1963. doi: 10.1175/1520-0493(1963)091<0099:GCEWTP>2.3.CO;2.

J. M. Stockie. The mathematics of atmospheric dispersion modeling. *SIAM Review*, 53(2):349–372, 2011. doi: 10.1137/10080991X.

R.B. Stull. *An introduction to boundary layer meteorology*. Kluver Academic Publishers, 1988. doi: 10.1007/978-94-009-3027-8.

F. Toja-Silva, C. Pregel-Hoderlein, and J. Chen. On the urban geometry generalization for cfd simulation of gas dispersion from chimneys: Comparison with gaussian plume model. *Journal of Wind Engineering and Industrial Aerodynamics*, 177:1–18, 2018. ISSN 0167-6105. doi: 10.1016/j.jweia.2018.04.003.

Y. Tominaga and T. Stathopoulos. Cfd simulation of near-field pollutant dispersion in the urban environment: A review of current modeling techniques. *Atmospheric Environment*, 79:716–730, 2013. ISSN 1352-2310. doi: 10.1016/j.atmosenv.2013.07.028.

B.D. Turner and R.H. Schulze. *Practical guide to atmsopheric dispersion modelling*. AWMA/Trinity Consultants, 2007.

D. B. Turner. *Workbook of atmospheric dispersion estimates: an introduction to dispersion modeling*. CRC press, 1967.

S. van der Linden. *From Dutch Short-Lived to Antarctic Long-Lived Stable Boundary Layers.* PhD thesis, Delft University of Technology, 2020.

P.A.M. Witsenboer. Modelling the dispersion of air pollutants in rotterdam using dales. Master's thesis, Delft University of Technology, 2023.

L. Zhengtong, T. Ming, S. Liu, C. Peng, R. de Richter, W. Li, H. Zhang, and C. Wen. Review on pollutant dispersion in urban areas-part a: Effects of mechanical factors and urban morphology. *Building and Environment*, 190:107534, 2021. doi: 10.1016/j.buildenv.2020.107534.

A

Vertical profiles of u and v wind

Figures A.1 and A.2 present the vertical profiles of the west to east (u) and the south to north (v) wind components up to a height of 100 meters.
Examining the u wind profile, the u wind velocity is higher under neutral conditions up to approximately 50 meters. Beyond this height, the u wind velocity is greater in the stable and very stable boundary layers up to approximately 400 meters (see Figure 4.1). In Figure A.2, the v wind velocities are similar up to about 20 meters. Beyond this point, the v wind velocities are higher in stable and very stable conditions up to a height of about 100 meters.

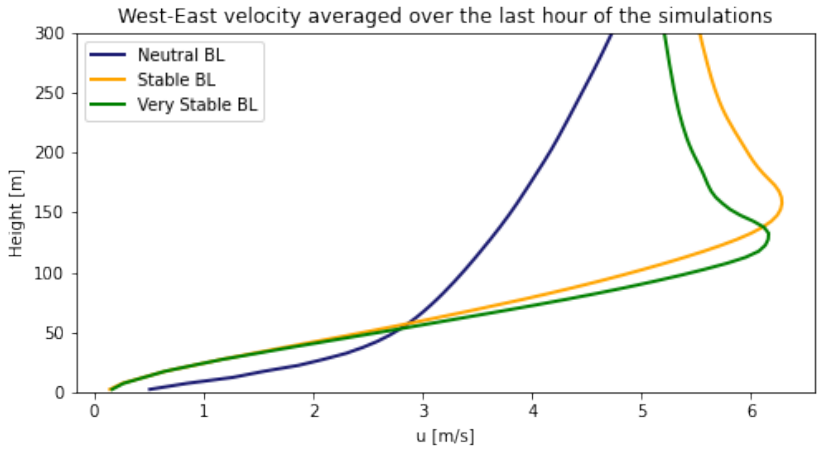

Figure A.1:
Vertical profile of the west to east (u) wind component under the three different atmospheric conditions. The vertical profile is plotted up to a height of 100 meters.

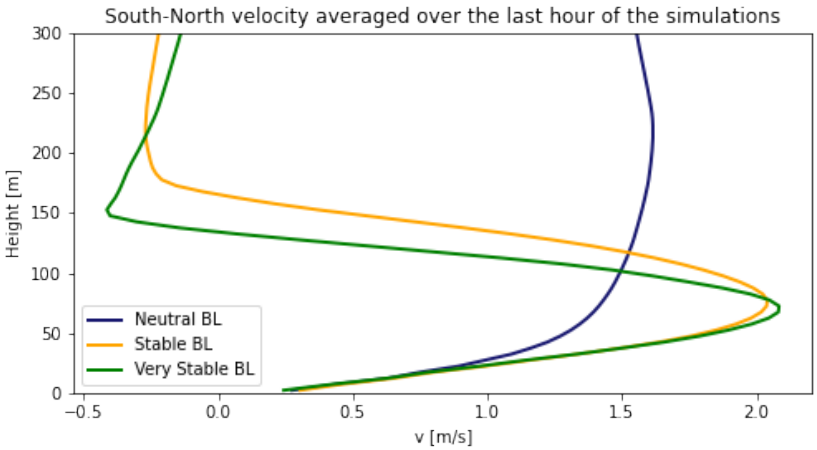

Figure A.2:
Vertical profile of the south to north (v) wind component under the three different atmospheric conditions. The vertical profile is plotted up to a height of 100 meters.

B

Rotated plume

Figure B.1 depicts the rotated plume in the new structured grid. 's' is the distance coordinate from the source along the direction of the wind, while 't' is the transverse coordinate. The buildings are also rotated along with the plume.

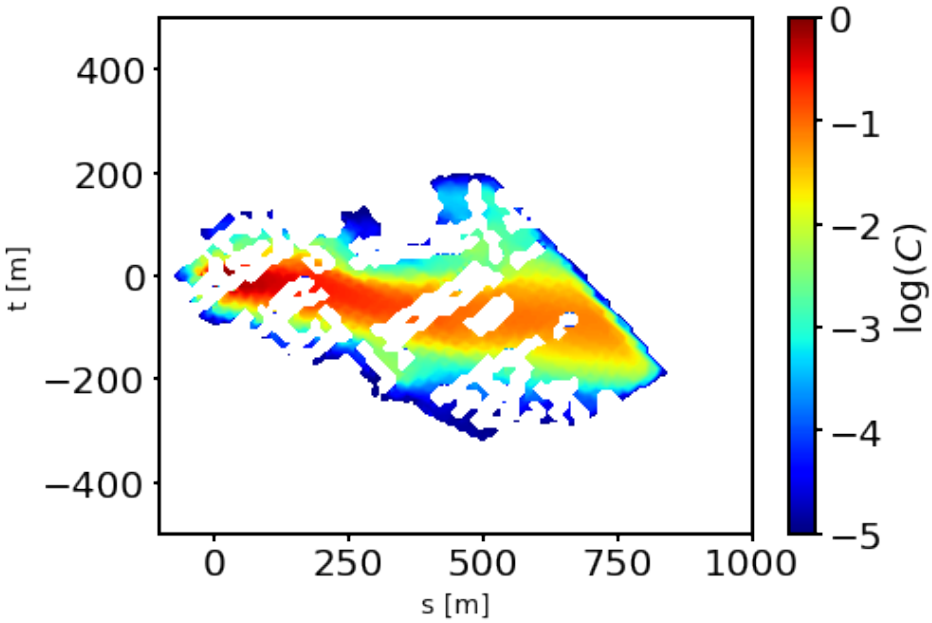

Figure B.1:
Rotated plume along the wind direction in the new (s,t) structured grid. Here, the plume from Source 1 under stable conditions is presented.

C

GPMs - Source 2

Figures C.1, C.2, and C.3 compare the simulations with the Gaussian plume models for Source 2. In the top row, DALES is displayed on the left and Cramer on the right. In the bottom row, Briggs is on the left and McElroy on the right. The observations align with previous comments: lower concentrations are observed under neutral and stable conditions in the GPMs compared to DALES, likely due to the initial lower concentrations shown in Table 4.4. Specifically, for Briggs, very fast decay rates are noted under neutral and stable conditions compared to Source 1.

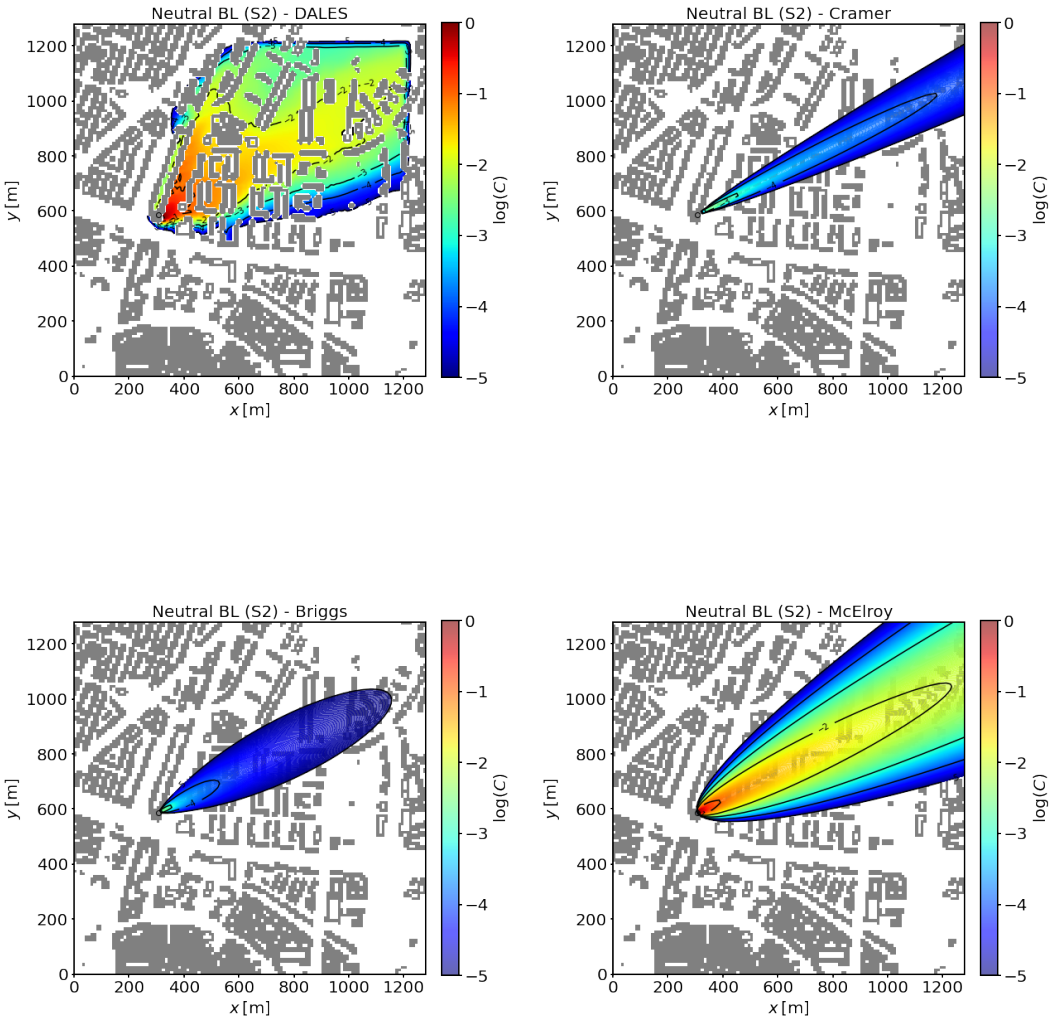

Figure C.1:
Comparison between DALES and Gaussian plume models for Source 2, under neutral conditions. Top row: DALES (left) and GPM using the scheme by **Cramer [1979]** (right). Bottom row: GPM using the schemes by **Briggs [1973]** (left) and by **McElroy and Pooler [1968]** (right).

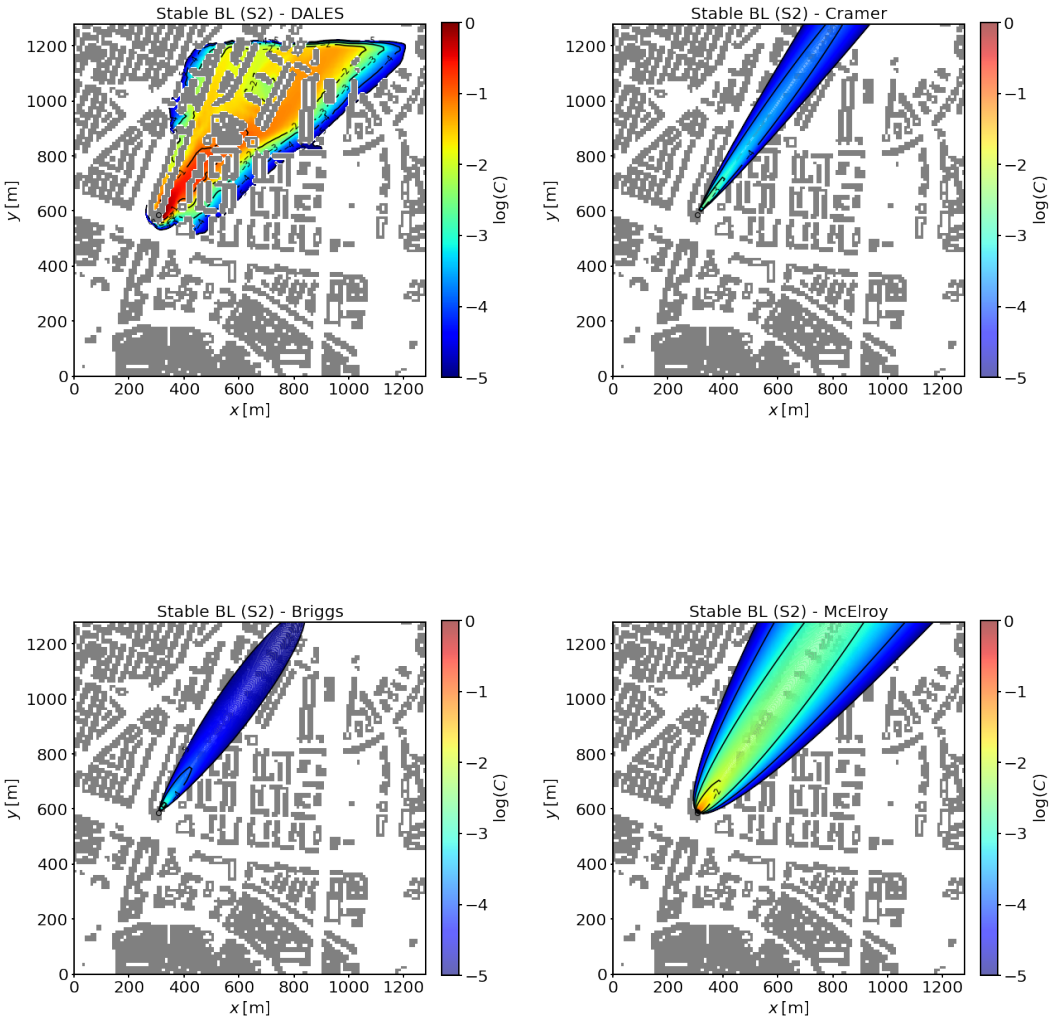

Figure C.2:
Comparison between DALES and Gaussian plume models for Source 2, under stable conditions. Top row: DALES (left) and GPM using the scheme by **Cramer [1979]** (right). Bottom row: GPM using the schemes by **Briggs [1973]** (left) and by **McElroy and Pooler [1968]** (right).

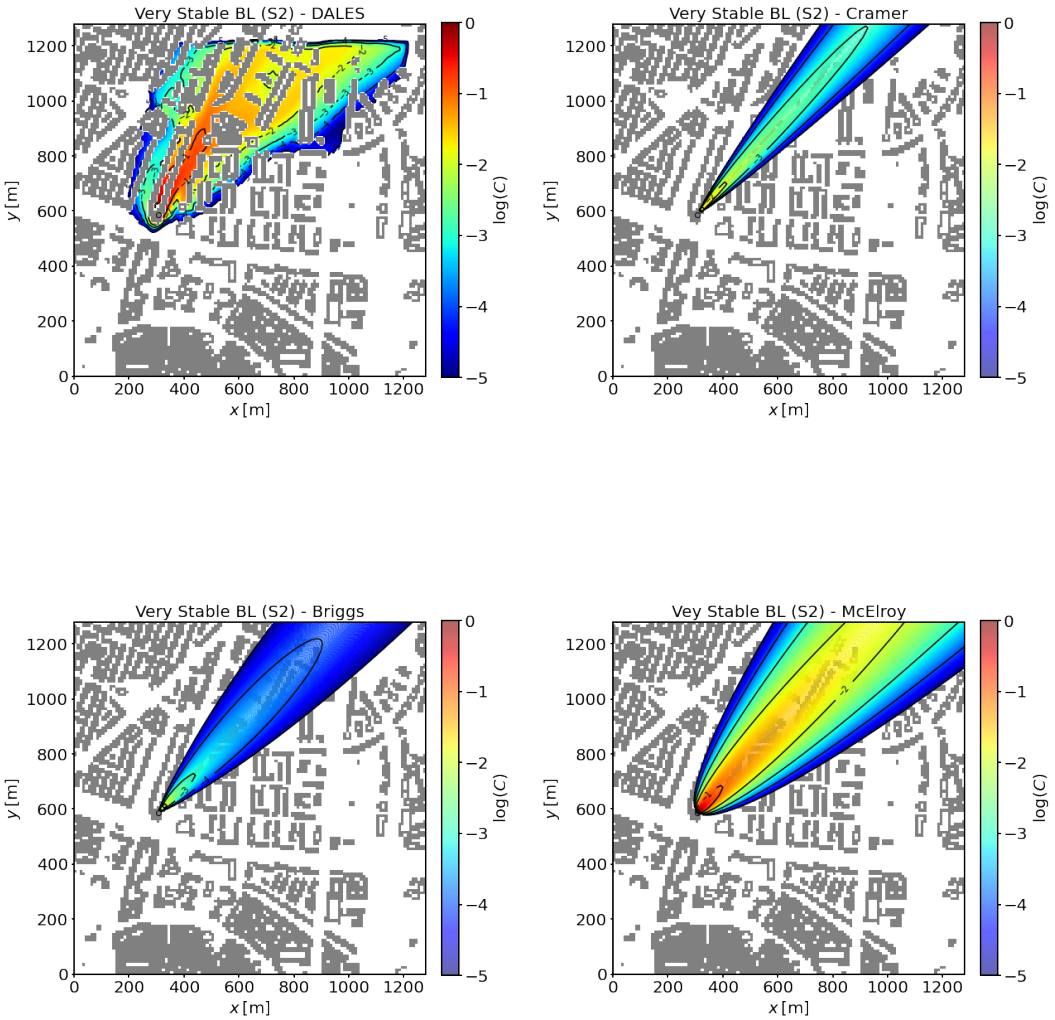

Figure C.3:
Comparison between DALES and Gaussian plume models for Source 2, under very stable conditions. Top row: DALES (left) and GPM using the scheme by **Cramer [1979]** (right). Bottom row: GPM using the schemes by **Briggs [1973]** (left) and by **McElroy and Pooler [1968]** (right).